SANDIA REPORT

SAND2009-0798
Unlimited Release
Printed February 2009

Investigating the Point Seismic Array Concept With Seismic Rotation Measurements

David F. Aldridge and Robert E. Abbott

Prepared by
Sandia National Laboratories
Albuquerque, New Mexico 87185 and Livermore, California 94550

Sandia is a multiprogram laboratory operated by Sandia Corporation,
a Lockheed Martin Company, for the United States Department of Energy's
National Nuclear Security Administration under Contract DE-AC04-94AL85000.

Sandia National Laboratories

Issued by Sandia National Laboratories, operated for the United States Department of Energy by Sandia Corporation.

Available to DOE and DOE contractors from
U.S. Department of Energy
Office of Scientific and Technical Information
P.O. Box 62
Oak Ridge, TN 37831

Telephone: (865) 576-8401
Facsimile: (865) 576-5728
E-Mail: reports@adonis.osti.gov
Online ordering: http://www.osti.gov/bridge

Available to the public from
U.S. Department of Commerce
National Technical Information Service
5285 Port Royal Rd.
Springfield, VA 22161

Telephone: (800) 553-6847
Facsimile: (703) 605-6900
E-Mail: orders@ntis.fedworld.gov
Online order: http://www.ntis.gov/help/ordermethods.asp?loc=7-4-0#online

SAND2009-0798
Unlimited Release
Printed February 2009

INVESTIGATING THE POINT SEISMIC ARRAY CONCEPT WITH SEISMIC ROTATION MEASUREMENTS

David F. Aldridge
Geophysics Department
Sandia National Laboratories
Albuquerque, New Mexico, USA, 87185-0750

Robert E. Abbott
Dynamic Material Properties Department
Sandia National Laboratories
Albuquerque, New Mexico, USA, 87185-1195

ABSTRACT

Spatially-distributed arrays of seismometers are often utilized to infer the speed and direction of incident seismic waves. Conventionally, individual seismometers of the array measure one or more orthogonal components of rectilinear particle motion (displacement, velocity, or acceleration). The present work demonstrates that measurement of *both* the particle velocity vector and the particle rotation vector at a *single* point receiver yields sufficient information to discern the type (compressional or shear), speed, and direction of an incident plane seismic wave. Hence, the approach offers the intriguing possibility of dispensing with spatially-extended receiver arrays, with their many problematic deployment, maintenance, relocation, and post-acquisition data processing issues. This study outlines straightforward mathematical theory underlying the point seismic array concept, and implements a simple cross-correlation scanning algorithm for determining the azimuth of incident seismic waves from measured acceleration and rotation rate data. The algorithm is successfully applied to synthetic seismic data generated by an advanced finite-difference seismic wave propagation modeling algorithm. Application of the same azimuth scanning approach to data acquired at a site near Yucca Mountain, Nevada yields ambiguous, albeit encouraging, results. Practical issues associated with rotational seismometry are recognized as important, but are not addressed in this investigation.

ACKNOWLEDGEMENTS

Sandia National Laboratories is a multiprogram science and engineering facility operated by Sandia Corporation, a Lockheed-Martin company, for the United States Department of Energy, National Nuclear Security Administration, under contract DE-AC04-94AL8500.

Results reported herein were obtained under the Sandia National Laboratories (SNL) Laboratory Directed Research and Development (LDRD) project entitled "Investigating the Point Seismic Array for Superior Seismic Monitoring". The Principal Investigator was Dr. David F. Aldridge (Geophysics Department), and the project team included (in alphabetical order) Dr. Robert E. Abbott (Dynamic Material Properties Department), Dr. Nedra Bonal (Geophysics Department), Mr. Darren Hart (Ground-Based Monitoring Research and Engineering Department), and Dr. Neill P. Symons (Geophysics Department). Finally, SNL management support for this work from Dr. Gregory J. Elbring (Geophysics Department) and Dr. K. Terry Stalker (Exploratory Real-Time Systems Department) is gratefully acknowledged.

We thank Mr. Robert H. Brune, a Colorado-based geophysical consultant with extensive experience in the petroleum exploration and geophysical contracting industries, for assessing the current "state of art and practice" of rotational seismometry.

CONTENTS

1.0 INTRODUCTION

There is growing interest within the seismological community in measuring and analyzing rotational motions associated with seismic waves propagating within the Earth. Conventional seismological measurements entail recording three orthogonal components of rectilinear particle motion (e.g., displacement, velocity, or acceleration) at a receiver location. Additional information is provided by detecting and recording rotations about these same three axes. As Figure 1.1 indicates, these rotations are analogous to pitch, roll, and yaw of an airplane or boat. Rotational seismometry is currently in its infancy, and the ability of make high-fidelity, broadband, point measurements of three-component (3C) rotational motions is limited. However, seismologists have recognized two significant benefits that would accrue from successful recording of rotations:

1) Seismic wavefield decomposition: A rotational motion sensor is capable of detecting and isolating shear (S) waves within the total seismic wavefield. Present generation geophones record both the compressional (P) and shear (S) waves that arrive (simultaneously or sequentially) at a receiver. Post-acquisition processing is used to decompose the recorded data into its constituent P and S components. These approaches are time consuming (and thus costly), and require specialized processing algorithms and human expertise. Also, the algorithms often rely on assumptions that may not hold in practice. If seismic wavefield decomposition could be effected by routine field measurements, then efficiencies would be achieved and costs lowered.

2) Point seismic array: Conventionally, spatially-extended arrays of seismometers are used to infer the speed, direction, and type (P or S) of an incident seismic wave. However, it can be theoretically demonstrated that all of these attributes can be determined by measuring the three components of particle velocity *together* with the three components of particle rotation at a *single* point receiver. Hence, the spatially-distributed array, with all of its attendant operational problems, can be dispensed with. This is an important issue in certain contexts (like covert intelligence gathering, or military operations) where speed of field deployment and safety of personnel are paramount.

Figure 1.2 graphically compares a circular array of 3C seismometers with the proposed "point seismic array" approach. As a plane wavefront sweeps across the array of sensors, individual recordings of translational ground motion are obtained. These data are then processed to infer the salient characteristics (wave type, speed, polarization and propagation directions) of the incident seismic wave. However, accurate inferences depend critically on uniformity of ground coupling, sensitivity axis orientations, and seismometer electromechanical responses (Aldridge, 1989). Moreover, variation in ground properties over the spatial extent of the array will degrade performance. All of these problems can be circumvented by emplacing a "six component sensor", measuring the three orthogonal components of translational *and* rotational motions, at a single point.

In this study, we utilize a combination of mathematical, numerical simulation, and field data acquisition methods to investigate the feasibility of the point seismic array concept. After deriving the theoretical basis of the point seismic array, we develop a simple data processing algorithm for inferring the azimuth and speed of an incident plane wave from co-located observations of particle velocity and rotation. The algorithm is successfully applied to realistic synthetic seismic data calculated for a layered earth model representing a site near Yucca Mountain, Nevada. Application of the algorithm to field data recorded at this same site yields ambiguous, although highly encouraging, results.

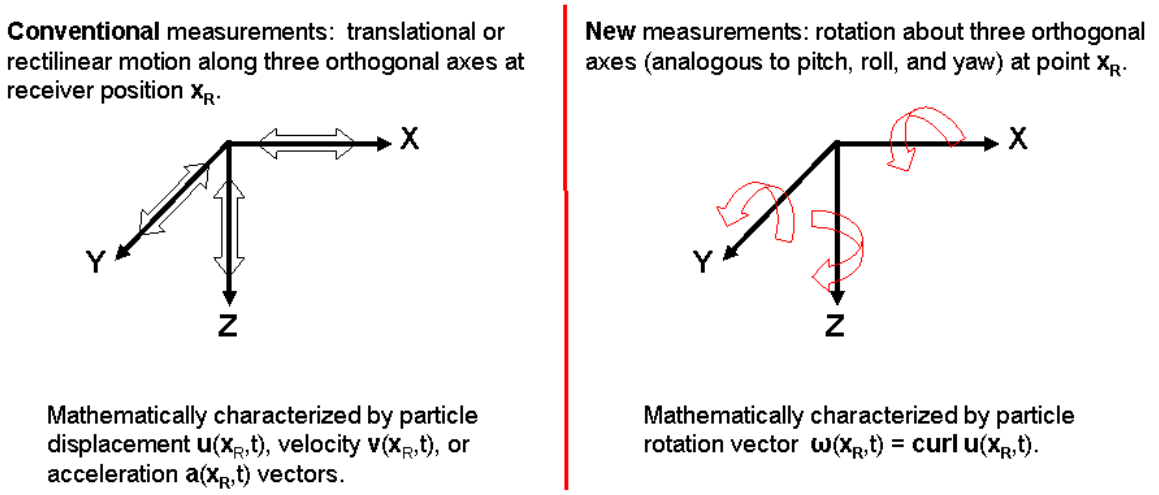

Figure 1.1. Graphic depictions of conventional (left panel) and new (right panel) three-component motions observed by seismometers.

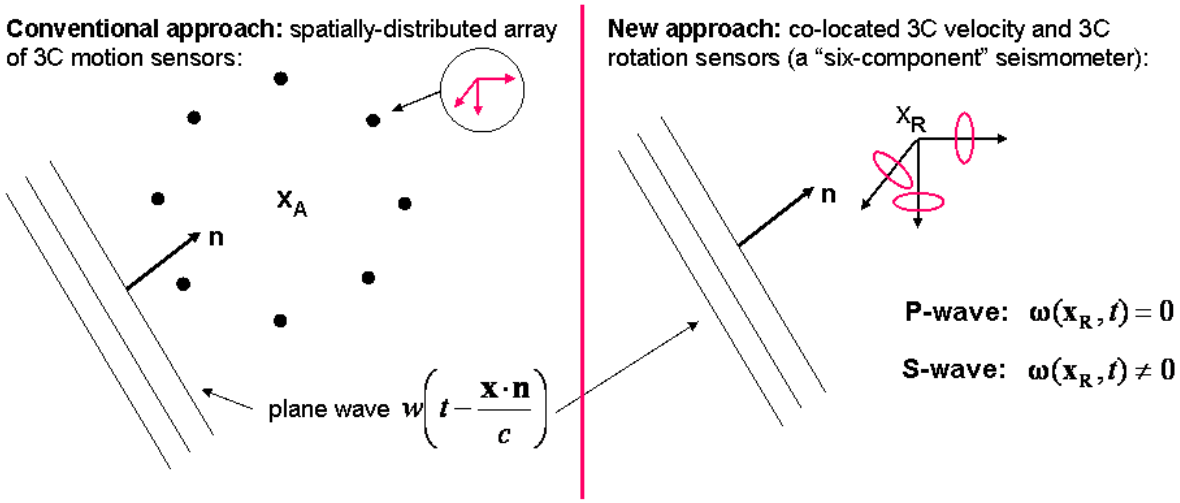

Figure 1.2. Comparison of a circular array (centered at $\mathbf{x}_A$) of three-component (3C) seismometers (left panel) with a "point seismic array" consisting of a 3C translational motion sensor co-located with a 3C rotational motion sensor at position $\mathbf{x}_R$. A train of plane seismic wavefronts propagates with speed c in the direction of unit vector $\mathbf{n}$. Measurement of the rotation vector $\boldsymbol{\omega}(\mathbf{x}_R,t)$ identifies the type (P or S) of incident wave.

2.0 MATHEMATICAL THEORY

In this section, we establish basic theoretical results underpinning the point seismic array concept. For mathematical tractability, several simplifying assumptions regarding wave propagation and medium properties are adopted. However, we do not consider these assumptions to be unreasonably restrictive.

2.1 Definitions

The *particle rotation vector* **r** is defined as the **curl** of the particle displacement vector **u**:

$$\mathbf{r}(\mathbf{x},t) \equiv \mathbf{curl}\ \mathbf{u}(\mathbf{x},t), \tag{2.1}$$

where **x** is the three-dimensional position vector and t is time. In Cartesian (x, y, z) coordinates, the components of the rotation vector are given by

$$r_x(\mathbf{x},t) = \frac{\partial u_z(\mathbf{x},t)}{\partial y} - \frac{\partial u_y(\mathbf{x},t)}{\partial z}, \tag{2.2a}$$

$$r_y(\mathbf{x},t) = \frac{\partial u_x(\mathbf{x},t)}{\partial z} - \frac{\partial u_z(\mathbf{x},t)}{\partial x}, \tag{2.2b}$$

$$r_z(\mathbf{x},t) = \frac{\partial u_y(\mathbf{x},t)}{\partial x} - \frac{\partial u_x(\mathbf{x},t)}{\partial y}. \tag{2.2c}$$

Thus, the rotation components are a particular linear combination of the space partial derivatives of the displacement components.

The (scalar-valued) *divergence d* of the particle displacement vector **u** is defined as

$$d(\mathbf{x},t) \equiv \mathrm{div}\ \mathbf{u}(\mathbf{x},t), \tag{2.3}$$

Hence, in Cartesian coordinates

$$d(\mathbf{x},t) = \frac{\partial u_x(x,t)}{\partial x} + \frac{\partial u_y(\mathbf{x},t)}{\partial y} + \frac{\partial u_z(\mathbf{x},t)}{\partial z}. \tag{2.4}$$

Divergence is a different linear combination of partial derivatives of displacement. Equations (2.2) and (2.4) motivate considering a general linear superposition of the nine displacement gradient tensor components $\partial u_i / \partial x_j$. Indices i, j = 1,2,3 refer to the three rectangular Cartesian coordinate directions x, y, and z, respectively. Let this (scalar-valued) superposition be designated by the (currently unnamed!) quantity

$$g(\mathbf{x},t) \equiv c_{ij} \frac{\partial u_i(\mathbf{x},t)}{\partial x_j}, \tag{2.5}$$

where c_{ij} are weight values, and repeated subscripts imply summation. Then, particle displacement divergence is obtained when the weights are given by

$$\begin{bmatrix} c_{11} & c_{12} & c_{13} \\ c_{21} & c_{22} & c_{23} \\ c_{31} & c_{32} & c_{33} \end{bmatrix} = \begin{bmatrix} 1 & 0 & 0 \\ 0 & 1 & 0 \\ 0 & 0 & 1 \end{bmatrix} \quad \Rightarrow \quad g(\mathbf{x},t) = d(\mathbf{x},t). \tag{2.6a}$$

The weighting matrix is isotropic (i.e., diagonal, and all diagonal elements equal). The x, y, and z components of particle rotation are obtained by specifying the weights as

$$\begin{bmatrix} c_{11} & c_{12} & c_{13} \\ c_{21} & c_{22} & c_{23} \\ c_{31} & c_{32} & c_{33} \end{bmatrix} = \begin{bmatrix} 0 & 0 & 0 \\ 0 & 0 & -1 \\ 0 & +1 & 0 \end{bmatrix} \quad \Rightarrow \quad g(\mathbf{x},t) = r_x(\mathbf{x},t), \tag{2.6b}$$

$$\begin{bmatrix} c_{11} & c_{12} & c_{13} \\ c_{21} & c_{22} & c_{23} \\ c_{31} & c_{32} & c_{33} \end{bmatrix} = \begin{bmatrix} 0 & 0 & +1 \\ 0 & 0 & 0 \\ -1 & 0 & 0 \end{bmatrix} \quad \Rightarrow \quad g(\mathbf{x},t) = r_y(\mathbf{x},t), \tag{2.6c}$$

$$\begin{bmatrix} c_{11} & c_{12} & c_{13} \\ c_{21} & c_{22} & c_{23} \\ c_{31} & c_{32} & c_{33} \end{bmatrix} = \begin{bmatrix} 0 & -1 & 0 \\ +1 & 0 & 0 \\ 0 & 0 & 0 \end{bmatrix} \quad \Rightarrow \quad g(\mathbf{x},t) = r_z(\mathbf{x},t). \tag{2.6d}$$

Each weight matrix is anti-symmetric (i.e., $c_{ij} = -c_{ji}$).

Equations (2.2) and (2.4) suggest a method for measuring rotation and divergence of seismic waves. If the displacement gradient tensor components $\partial u_i / \partial x_j$ can be measured, then rotation and divergence are readily constructed by forming the requisite linear combinations. Other, more general, linear combinations of the displacement gradient tensor components can be contemplated (as per equation (2.5)), although their seismological utility is presently unknown. One potentially viable approach for estimating the displacement gradient tensor components is to form differences of the displacement components in the three coordinate directions, over small spatial intervals. Engineering and transduction issues associated with obtaining such measurements with high fidelity are beyond the scope of the present report.

Pressure is commonly recorded in seismic and/or acoustic wave propagation experiments. Pressure is proportional to the divergence of the particle displacement vector, as follows

$$p(\mathbf{x},t) = -\kappa(\mathbf{x}) \operatorname{div} \mathbf{u}(\mathbf{x},t) = -\kappa(\mathbf{x})\, d(\mathbf{x},t), \tag{2.7}$$

where $\kappa(\mathbf{x})$ is the bulk modulus of the medium. Although pressure sensors are common, well-developed, and cheap, the fact that the medium parameter κ appears in the above relation presents an ambiguity for the point seismic array concept, as discussed below.

Finally, we remark that the definitions (2.1) and (2.3) are independent of the type of medium supporting seismic wave propagation (e.g., elastic, anelastic), the degree of spatial heterogeneity and anisotropy, as well as the geometry of a propagating seismic wavefront (e.g., plane or curved). However, in subsequent sections, we will specialize the analysis to plane or spherical wave propagation within homogeneous and isotropic media, for purposes of mathematical tractability.

2.2 Isotropic Elastic Media

Consider a three-dimensional isotropic elastic medium characterized by compressional (P) wavespeed α, shear (S) wavespeed β, and mass density ρ. Let ($\mathbf{e}_x$, $\mathbf{e}_y$, $\mathbf{e}_z$) be an orthonormal triad of basis vectors for three-dimensional space. Then, the position vector is given by $\mathbf{x} = x\mathbf{e}_x + y\mathbf{e}_y + z\mathbf{e}_z$ where (x, y, z) are spatial coordinates. Next, consider a plane elastic wave propagating in direction of unit vector **n** with speed c. The particle displacement vector $\mathbf{u}(\mathbf{x},t)$ associated with this wave is

$$\mathbf{u}(\mathbf{x},t) = U\mathbf{p}w\left(t - \frac{\mathbf{x}\cdot\mathbf{n}}{c}\right), \tag{2.8}$$

where U is a displacement amplitude scalar (dimension: length; SI unit: m), **p** is a dimensionless unit polarization vector, and $w(t)$ is the dimensionless displacement waveform. Wavelet $w(t)$ is typically normalized to unit maximum absolute amplitude: max $|w(t)| = 1$. For a compressional wave, $\mathbf{p} = \mathbf{n}$ and $c = \alpha$, where α is the P-wave speed characterizing the elastic medium. Particle motion polarization is longitudinal (parallel to the propagation direction **n**). For a plane shear wave, $\mathbf{p}\cdot\mathbf{n} = 0$ and $c = \beta$, where β is the elastic S-wave speed. S-wave particle motion is transverse to the propagation direction.

The particle velocity vector $\mathbf{v}(\mathbf{x},t) \equiv \partial\mathbf{u}(\mathbf{x},t)/\partial t$ associated with plane wave (2.8) is

$$\mathbf{v}(\mathbf{x},t) = U\mathbf{p}w'\left(t - \frac{\mathbf{x}\cdot\mathbf{n}}{c}\right), \tag{2.9}$$

where the prime denotes differentiation of a function with respect to its argument. The particle rotation vector $\mathbf{r}(\mathbf{x},t) \equiv \mathbf{curl}\ \mathbf{u}(\mathbf{x},t)$ associated with plane wave (2.8) is

$$\mathbf{r}(\mathbf{x},t) = -\frac{U}{c}(\mathbf{n}\times\mathbf{p})\, w'\left(t - \frac{\mathbf{x}\cdot\mathbf{n}}{c}\right). \tag{2.10}$$

Note that particle rotation is a dimensionless quantity, and is perpendicular to *both* **p** and **n**. Finally the divergence associated with the plane wave is $d(\mathbf{x},t) \equiv \mathrm{div}\ \mathbf{u}(\mathbf{x},t)$:

$$d(\mathbf{x},t) = -\frac{U}{c}(\mathbf{n}\cdot\mathbf{p})\, w'\left(t - \frac{\mathbf{x}\cdot\mathbf{n}}{c}\right). \tag{2.11}$$

Clearly, particle velocity **v**, particle rotation **r**, and divergence d all propagate in the same direction **n** as the particle displacement **u**, and with the same speed c. Each has a temporal waveform given by the derivative of the displacement waveform $w(t)$.

For a compressional wave, the particle rotation vanishes since $\mathbf{n} \times \mathbf{p} = \mathbf{n} \times \mathbf{n} = \mathbf{0}$, whereas for a shear wave the divergence vanishes since $\mathbf{n} \cdot \mathbf{p} = 0$. Hence, rotation and/or divergence measured at a point receiver at position $\mathbf{x}_R$ serves as an identifier of the type of incident elastic wave:

$$\mathbf{r}(\mathbf{x}_R, t) = \mathbf{0} \quad \text{and/or} \quad d(\mathbf{x}_R, t) \neq 0 \quad \Rightarrow \quad \text{incident P - wave at } \mathbf{x}_R ,$$

$$\mathbf{r}(\mathbf{x}_R, t) \neq \mathbf{0} \quad \text{and/or} \quad d(\mathbf{x}_R, t) = 0 \quad \Rightarrow \quad \text{incident S - wave at } \mathbf{x}_R .$$

Note that either observed quantity (rotation or divergence) *alone* is sufficient to establish the identity of the seismic wave. However, simultaneous use of both indicators is probably a more robust approach with field-acquired seismic data.

After the type of incident wave is identified, then the propagation direction and wavespeed are determined as follows.

***Plane Compressional (P) Wave*:**

For a plane P-wave, the polarization vector **p** equals the propagation direction vector **n**. Then, equation (2.9) above implies

$$\frac{\mathbf{v}(\mathbf{x}_R, t)}{\|\mathbf{v}(\mathbf{x}_R, t)\|} = \pm \mathbf{n}(\mathbf{x}_R). \tag{2.12}$$

Observed three-component particle velocity is sufficient to obtain the propagation direction (to within a sign factor). This is well-known. However, with an additional co-located measurement of displacement divergence, the compressional wavespeed at the receiver location may *also* be determined. From equations (2.9) and (2.11):

$$\frac{\|\mathbf{v}(\mathbf{x}_R, t)\|}{|d(\mathbf{x}_R, t)|} = \alpha(\mathbf{x}_R). \tag{2.13}$$

However, co-located observations of particle velocity and pressure are insufficient to determine the compressional wavespeed. Forming the ratio of particle velocity and pressure yields

$$\frac{\|\mathbf{v}(\mathbf{x}_R, t)\|}{|p(\mathbf{x}_R, t)|} = \frac{\alpha(\mathbf{x}_R)}{\kappa(\mathbf{x}_R)}. \tag{2.14}$$

Independent knowledge of bulk modulus $\kappa = \rho(\alpha^2 - 2\beta^2)$ at the receiver point is needed to infer P-wave speed α. Although pressure receivers are quite common, this particular deficiency strongly motivates development of the displacement divergence sensor (or the more general displacement gradient sensor of equation (2.5)).

***Plane Shear (S) Wave*:**

After a shear wave is identified, its propagation direction may be obtained from the vector cross product of particle rotation **ω** and particle velocity **v.** Using the well-known "Bac-Cab rule" for a triple vector product [$\mathbf{a} \times (\mathbf{b} \times \mathbf{c}) = \mathbf{b}(\mathbf{a} \cdot \mathbf{c}) - \mathbf{c}(\mathbf{a} \cdot \mathbf{b})$] , we obtain from equations (2.9) and (2.10) above:

$$\mathbf{r}(\mathbf{x},t)\times\mathbf{v}(\mathbf{x},t)=\frac{1}{c}\left[Uw'\left(t-\frac{\mathbf{x}\cdot\mathbf{n}}{c}\right)\right]^2\left[\mathbf{n}-(\mathbf{n}\cdot\mathbf{p})\mathbf{p}\right]. \tag{2.15}$$

For a shear wave $\mathbf{n}\cdot\mathbf{p}=0$, and the above cross product is oriented parallel to the propagation direction $\mathbf{n}$ of the plane wave:

$$\mathbf{r}(\mathbf{x},t)\times\mathbf{v}(\mathbf{x},t)=\frac{1}{\beta}\left[Uw'\left(t-\frac{\mathbf{x}\cdot\mathbf{n}}{\beta}\right)\right]^2\mathbf{n}\,, \tag{2.16}$$

where shear wavespeed $c=\beta$ is used. Thus, measurement of both $\mathbf{r}$ and $\mathbf{v}$ at the same receiver location $\mathbf{x}=\mathbf{x}_R$ enables, in principle, determination of the propagation direction $\mathbf{n}$ of an elastic shear wave incident upon that point! That is

$$\frac{\mathbf{r}(\mathbf{x}_R,t)\times\mathbf{v}(\mathbf{x}_R,t)}{\left\|\mathbf{r}(\mathbf{x}_R,t)\times\mathbf{v}(\mathbf{x}_R,t)\right\|}=\mathbf{n}(\mathbf{x}_R). \tag{2.17}$$

Moreover, there is *no* sign ambiguity regarding the direction of incident wave propagation, in contrast with the analogous situation for a P-wave (i.e., equation (2.12)). From equations (2.9) and (2.10) above, shear wavespeed β at the receiver position $\mathbf{x}_R$ is obtained from the ratio

$$\frac{\left\|\mathbf{v}(\mathbf{x}_R,t)\right\|}{\left\|\mathbf{r}(\mathbf{x}_R,t)\right\|}=\beta(\mathbf{x}_R). \tag{2.18}$$

The results developed above rigorously establish, at least in a theoretical or conceptual sense, that coincident recording of three-component (3C) particle velocity, 3C particle rotation, and displacement divergence at a single point $\mathbf{x}_R$ in space enables determination of the type (P or S), propagation direction, and speed of an incident seismic wave. To our knowledge, the analysis is novel. A major simplifying assumption entails plane wave propagation within a uniform (i.e., homogeneous) isotropic elastic medium. However, we do not consider this restriction to be overly limiting. Rather, medium properties at the receiver location only need to be *locally homogeneous*, and the incident seismic wavefront *locally plane*. Of course, the spatial extent of this local zone depends on the spectral content of the propagating wave: higher/lower frequencies imply a smaller/larger region.

An important generalization of the above favorable "point seismic array" conclusions exists for the case of *spherical* wave propagation, provided the curvature of the propagating wavefront is small (or alternatively, the receiver is located in the *far-field* of the seismic energy source). Mathematical formulae previously developed by Aldridge (2000) characterize the elastic wavefield (particle velocity, particle rotation, and pressure) generated by a point seismic energy source sited within a homogeneous and isotropic elastic wholespace. The source may be either a force density vector (SI unit: N/m^3) or a moment density tensor (SI unit: $N\text{-}m/m^3 = P$). Numerous seismic energy sources such as explosions, dipoles, couples, torques, shear and/or tensile dislocations, etc. are represented by a moment density tensor.

***Spherical Compressional (P) Wave*:**

For a spherical elastic P-wave diverging from a point seismic energy source, the particle rotation vanishes and the displacement divergence is non-zero:

$$\mathbf{r}(\mathbf{x}_R, t) = \mathbf{0} \quad \text{and} \quad d(\mathbf{x}_R, t) \neq 0 . \tag{2.19a}$$

Then, it is readily established from the applicable formulae in Aldridge (2000) that the far-field velocity vector and displacement divergence satisfy equations (2.12) and (2.13) above. That is:

$$\frac{\mathbf{v}_{far}(\mathbf{x}_R, t)}{\left\|\mathbf{v}_{far}(\mathbf{x}_R, t)\right\|} = \pm \mathbf{n}(\mathbf{x}_R), \qquad \frac{\left\|\mathbf{v}_{far}(\mathbf{x}_R, t)\right\|}{\left|d_{far}(\mathbf{x}_R, t)\right|} = \alpha(\mathbf{x}_R). \tag{2.19b,c}$$

The propagation direction and P-wave speed at a receiver may be inferred from measurements made at a single point $\mathbf{x}^R$. Note that the sign ambiguity remains in determining the unit direction vector **n**.

***Spherical Shear (S) Wave*:**

For a spherical elastic S-wave diverging from a point source in a uniform elastic wholespace, the particle rotation vector is non-zero, and the displacement divergence vanishes:

$$\mathbf{r}(\mathbf{x}_R, t) \neq \mathbf{0} \quad \text{and} \quad d(\mathbf{x}_R, t) = 0 . \tag{2.20a}$$

Then, analogues of equations (2.17) and (2.18) hold with the far-field rotation and velocity vectors:

$$\frac{\mathbf{r}_{far}(\mathbf{x}_R, t) \times \mathbf{v}_{far}(\mathbf{x}_R, t)}{\left\|\mathbf{r}_{far}(\mathbf{x}, t) \times \mathbf{v}_{far}(\mathbf{x}_R, t)\right\|} = \mathbf{n}(\mathbf{x}_R), \qquad \frac{\left\|\mathbf{v}_{far}(\mathbf{x}_R, t)\right\|}{\left\|\mathbf{r}_{far}(\mathbf{x}_R, t)\right\|} = \beta(\mathbf{x}_R). \tag{2.20b,c}$$

Once again, propagation direction (with no sign ambiguity) and S-wave speed of an incident shear wave may be determined.

We emphasize that these results rigorously apply at far-field distances from the point seismic energy source. If the receiver is close to the source point, wavefront curvature is significant, and the near- and intermediate-field terms in the wavefield formulae of Aldridge (2000) must be taken into account. Interestingly, these same formulae demonstrate that the particle velocity vector and particle rotation vector are orthogonal, *at all distances* from a point seismic energy source:

$$\mathbf{r}(\mathbf{x}, t) \cdot \mathbf{v}(\mathbf{x}, t) = 0 , \tag{2.21}$$

where $\left\|\mathbf{x} - \mathbf{x}_S\right\|$ can be any distance. At any position **x**, the particle rotation vector **r**(**x**,*t*) of a diverging spherical elastic wave is contained in the time-varying plane perpendicular to the particle velocity vector **v**(**x**,*t*). [For plane P or S elastic waves, condition (2.21) trivially holds, as can be established from equations (2.9) and (2.10) above.] This deduction (which we consider to be unfamiliar to seismologists) may provide a clue regarding how to construct a particle rotation sensor.

2.3 Isotropic Anelastic Media

Seismometers are commonly sited on or within geologic media at or near the earth's surface (e.g., soils, sands, gravels, unconsolidated alluvium, etc.) that are highly attenuating for seismic wave propagation. A recurring question during this project has been "What is the effect of attenuation on the ability of the point seismic array to estimate incident wave propagation properties?" In this section, we demonstrate that coincident recordings of particle velocity, particle rotation, and displacement divergence again enable the type, direction, and wavespeed of an incident wave to be determined. For mathematical simplicity, plane wave propagation within an isotropic anelastic (i.e., attenuative and dispersive) medium is assumed. One complicating issue is that seismic wavespeed depends on frequency.

Consider a plane particle displacement wave propagating in the direction of unit vector **n** within a homogeneous and isotropic anelastic medium. The wave is polarized in the direction of unit vector **p**. As with elastic (i.e., non-attenuating) plane waves, **p** = **n** for P-waves and **p** is perpendicular to **n** for S-waves. As the wave progresses, its waveform continuously changes shape due to dispersion. If $w(t)$ is the waveform at a reference point (here taken to be the coordinate origin), then the particle displacement at position **x** is given by

$$\mathbf{u}(\mathbf{x},t) = U\mathbf{p}\left[w(t) * f(\mathbf{x},t;\mathbf{n})\right], \tag{2.22}$$

where the asterisk denotes convolution with respect to the time variable t. U is a displacement amplitude scalar, and function $f(\mathbf{x},t;\mathbf{n})$ is given by the inverse Fourier transform relation

$$f(\mathbf{x},t;\mathbf{n}) \equiv \frac{1}{2\pi}\int_{-\infty}^{+\infty} \exp\left[+iK(\omega)(\mathbf{x}\cdot\mathbf{n})\right]\exp\left[-i\omega t\right]d\omega\,. \tag{2.23}$$

Quantity $K(\omega)$ in the integrand of (2.23) is a function of angular frequency ω and is called the *complex wavenumber*. The real and imaginary parts of the complex wavenumber include the *phase speed* $c(\omega)$ and the *attenuation factor* $h(\omega)$:

$$K(\omega) = \frac{\omega}{c(\omega)} + ih(\omega)\,. \tag{2.24}$$

In the pure elastic case, the attenuation factor vanishes ($h(\omega) = 0$) and the phase speed becomes independent of angular frequency ($c(\omega) = c$). Then, the inverse Fourier transform (2.23) can be evaluated analytically, and function $f(\mathbf{x},t;\mathbf{n})$ reduces to a time-shifted Dirac delta function:

$$f(\mathbf{x},t;\mathbf{n}) \to \delta\left(t - \frac{\mathbf{x}\cdot n}{c}\right). \tag{2.25}$$

Combining equation (2.25) with (2.22) then gives the proper form (2.8) for a plane elastic wave.

The particle velocity vector is obtained by differentiating (2.22) with respect to time:

$$\mathbf{v}(\mathbf{x},t) \equiv \frac{\partial \mathbf{u}(\mathbf{x},t)}{\partial t} = U\mathbf{p}\left[w'(t) * f(\mathbf{x},t;\mathbf{n})\right]. \tag{2.26}$$

Particle rotation and displacement divergence are given by

$$\mathbf{r}(\mathbf{x},t) \equiv \mathbf{curl}\,\mathbf{u}(\mathbf{x},t) = -U(\mathbf{n}\times\mathbf{p})\left[w(t) * e(\mathbf{x},t;\mathbf{n})\right], \tag{2.27}$$

and

$$d(\mathbf{x},t) \equiv \mathrm{div}\,\mathbf{u}(\mathbf{x},t) = -U(\mathbf{n}\cdot\mathbf{p})\left[w(t) * e(\mathbf{x},t;\mathbf{n})\right], \tag{2.28}$$

respectively. The space- and time-dependent function $e(\mathbf{x},t;\mathbf{n})$ in these expressions is the inverse Fourier transform

$$e(\mathbf{x},t;\mathbf{n}) \equiv \frac{1}{2\pi}\int_{-\infty}^{+\infty}\left[-iK(\omega)\right]\exp\left[+iK(\omega)(\mathbf{x}\cdot\mathbf{n})\right]\exp\left[-i\omega t\right]d\omega\,. \tag{2.29}$$

In the pure elastic case, $e(\mathbf{x},t;\mathbf{n})$ reduces to

$$e(\mathbf{x},t;\mathbf{n}) \to \frac{1}{c}\delta'\left(t-\frac{\mathbf{x}\cdot\mathbf{n}}{c}\right), \tag{2.30}$$

where a prime indicates differentiation of a function with respect to its argument. Hence, expressions (2.27) and (2.28) reduce to the appropriate forms of rotation and displacement divergence for plane elastic waves.

***Wave Type*:**

The basic time-domain description of plane anelastic wave propagation is now in place. In *exactly* the same manner as with elastic waves, the particle rotation vanishes for a compressional wave (since $\mathbf{n}\times\mathbf{p} = \mathbf{n}\times\mathbf{n} = \mathbf{0}$) and the divergence vanishes for a shear wave (since $\mathbf{n}\cdot\mathbf{p} = 0$). Hence, rotation and/or divergence measured at a point receiver at position $\mathbf{x}_R$ identifies of the type of incident anelastic wave:

$$\mathbf{r}(\mathbf{x}_R,t) = \mathbf{0} \quad \text{and/or} \quad d(\mathbf{x}_R,t) \neq 0 \quad \Rightarrow \quad \text{incident P - wave at } \mathbf{x}_R\,,$$

$$\mathbf{r}(\mathbf{x}_R,t) \neq \mathbf{0} \quad \text{and/or} \quad d(\mathbf{x}_R,t) = 0 \quad \Rightarrow \quad \text{incident S - wave at } \mathbf{x}_R\,.$$

Seismic wave attenuation and dispersion do not diminish the ability of rotation and/or divergence measurements to distinguish the type of wave arriving at a single point receiver.

***Propagation Direction*:**

From equation (2.26), for a P-wave where $\mathbf{p} = \mathbf{n}$, the normalized 3C particle velocity vector observed at the receiver point $\mathbf{x}_R$ is parallel to the unit propagation vector:

$$\frac{\mathbf{v}(\mathbf{x}_R,t)}{\left\|\mathbf{v}(\mathbf{x}_R,t)\right\|} = \pm\,\mathbf{n}(\mathbf{x}_R)\,. \tag{2.31}$$

For an S-wave, form the cross product of the rotation and velocity vectors (and utilize the "Bac-Cab" rule) to obtain:

$$\mathbf{r}(\mathbf{x},t)\times\mathbf{v}(\mathbf{x},t)=U^2\left[w(t)*e(\mathbf{x},t;\mathbf{n})\right]\left[w'(t)*f(\mathbf{x},t;\mathbf{n})\right]\mathbf{n}\,.$$

Then, normalizing and evaluating at the receiver position $\mathbf{x}_R$ gives

$$\frac{\mathbf{r}(\mathbf{x}_R,t)\times\mathbf{v}(\mathbf{x}_R,t)}{\left\|\mathbf{r}(\mathbf{x}_R,t)\times\mathbf{v}(\mathbf{x}_R,t)\right\|}=\pm\,\mathbf{n}(\mathbf{x}_R)\,. \tag{2.32}$$

Thus, expressions (2.31) and (2.32) imply that propagation direction may also be inferred at the receiver point, which is identical to the situation with plane elastic waves (as per the previous equations (2.12) and (2.17)). Curiously, we detect a sign ambiguity associated with the S-wave propagation direction, in contrast to the case for plane elastic waves (2.17).

***Propagation Speed*:**

Determination of the propagation speeds of plane anelastic waves is facilitated by performing the analysis in the frequency-domain. The above expressions for displacement, velocity, rotation, and divergence are Fourier transformed on time t to angular frequency ω. Upper case symbols refer to (complex-valued) Fourier transforms of (real-valued) lower case counterparts. Thus, the Fourier transform of the particle displacement vector (2.22) is

$$\mathbf{U}(\mathbf{x},\omega)=U\mathbf{p}W(\omega)\exp\left[+iK(\omega)(\mathbf{x}\cdot\mathbf{n})\right], \tag{2.33a}$$

where $W(\omega)$ is the Fourier spectrum of the time-domain wavelet w(t). Likewise, transforms of velocity, rotation, and divergence are

$$\mathbf{V}(\mathbf{x},\omega)\equiv -i\omega\,\mathbf{U}(\mathbf{x},\omega)=-i\omega\,U\mathbf{p}W(\omega)\exp\left[+iK(\omega)(\mathbf{x}\cdot\mathbf{n})\right], \tag{2.33b}$$

$$\mathbf{R}(\mathbf{x},\omega)\equiv\mathbf{curl}\;\mathbf{U}(\mathbf{x},\omega)=iK(\omega)\,U(\mathbf{n}\times\mathbf{p})W(\omega)\exp\left[+iK(\omega)(\mathbf{x}\cdot\mathbf{n})\right], \tag{2.33c}$$

$$D(\mathbf{x},\omega)\equiv\mathrm{div}\;\mathbf{U}(\mathbf{x},\omega)=iK(\omega)U\,(\mathbf{n}\cdot\mathbf{p})W(\omega)\exp\left[+iK(\omega)(\mathbf{x}\cdot\mathbf{n})\right]. \tag{2.33d}$$

Although there are various ways to proceed with these frequency-domain expressions, we form the ratio of magnitudes of particle velocity and displacement divergence spectra, analogous to the previous time-domain equation (2.13). Thus, for a plane P-wave ($\mathbf{p}=\mathbf{n}$):

$$\frac{\left\|\mathbf{V}(\mathbf{x},\omega)\right\|}{\left\|D(\mathbf{x},\omega)\right\|}=\frac{|\omega|}{\left\|K_\alpha(\omega)\right\|}=\alpha(\omega)\left[1+\left(\frac{\alpha(\omega)h_\alpha(\omega)}{\omega}\right)^2\right]^{-1/2}, \tag{2.34}$$

where $\alpha(\omega)$ is the frequency-dependent compressional phase speed. The ratio depends on the P-wave attenuation factor $h_\alpha(\omega)$ in addition to the phase speed. However, from the information in Figures 2.1 and 2.2 (from Schwaiger, Aldridge, and Haney, 2007) it is seen that, for typical geologic media, the magnitude of the factor $\alpha h/\omega$ is much less than unity. This quantity depends approximately on the *quality factor* $Q(\omega)$ characterizing anelastic wave propagation via

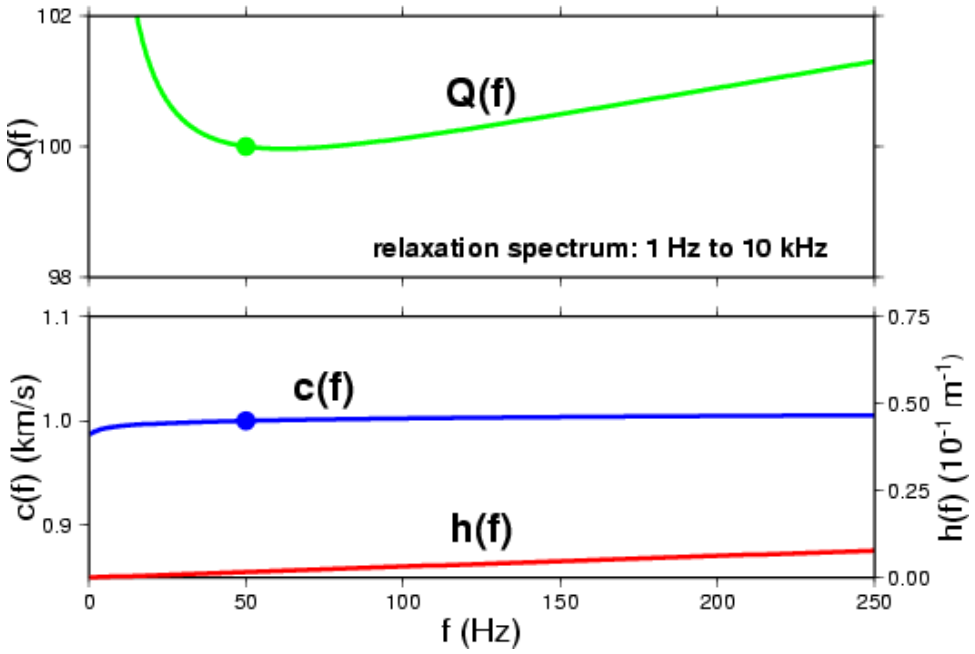

Figure 2.1. Quality factor Q (**green**), phase speed c (**blue**), and attenuation factor h (**red**) for a "high Q" anelastic medium characterized by a rectangular spectrum of relaxation mechanisms. Q and c at the reference frequency f = 50 Hz are taken to be 100 and 1000 m/s, respectively.

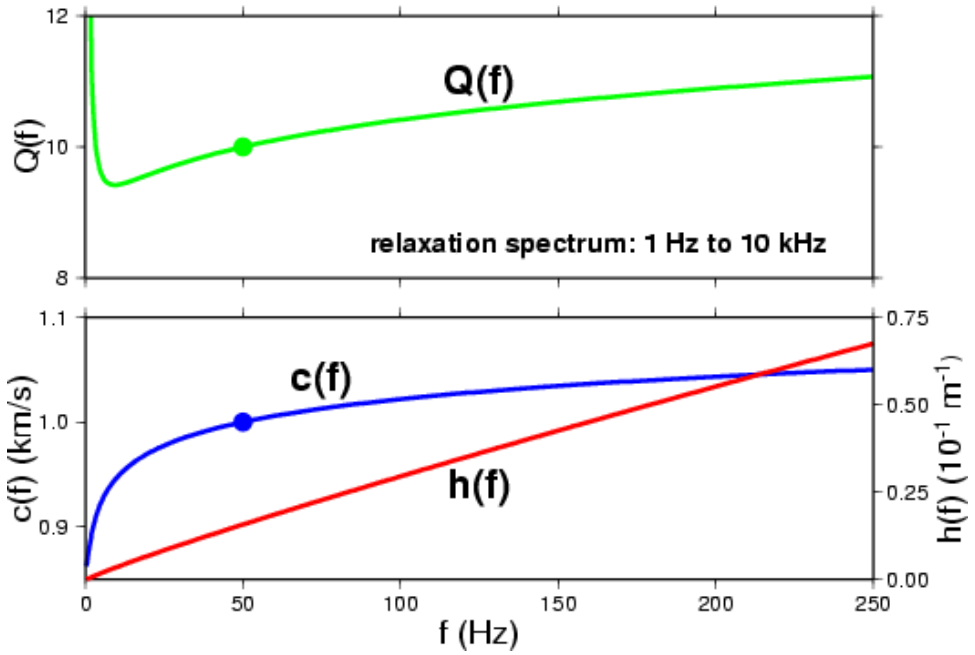

Figure 2.2. Quality factor Q (**green**), phase speed c (**blue**), and attenuation factor h (**red**) for a "low Q" anelastic medium characterized by a rectangular spectrum of relaxation mechanisms. Q and c at the reference frequency f = 50 Hz are taken to be 10 and 1000 m/s, respectively.

$$\frac{\alpha(\omega)h_{\alpha}(\omega)}{\omega} \approx \frac{1}{2Q_{\alpha}(\omega)},$$

(Ben-Menahem and Singh, 1981). Thus, to a high degree of accuracy, equation (2.34) is well-approximated by

$$\frac{\|\mathbf{V}(\mathbf{x},\omega)\|}{\|D(\mathbf{x},\omega)\|} \approx \alpha(\omega)\left[1-\frac{1}{8Q_{\alpha}(\omega)^2}\right]. \tag{2.35}$$

For example, for a low Q (i.e., highly attenuating) medium with $Q = 10$, the quantity in square brackets on the right side equals 0.99875. For higher Q, the factor is even closer to unity. Thus, it is safe to take the spectral magnitude ratio of particle velocity and displacement divergence equal to the frequency-dependent compressional phase speed at the receiver location:

$$\frac{\|\mathbf{V}(\mathbf{x}_R,\omega)\|}{\|D(\mathbf{x}_R,\omega)\|} \approx \alpha(\mathbf{x}_R,\omega). \tag{2.36}$$

For a plane anelastic S-wave, a similar analysis yields the following approximation for the ratio of particle velocity and particle rotation spectra:

$$\frac{\|\mathbf{V}(\mathbf{x}_R,\omega)\|}{\|\mathbf{R}(\mathbf{x}_R,\omega)\|} = \frac{|\omega|}{\|K_{\beta}(\omega)\|} \approx \beta(\omega)\left[1-\frac{1}{8Q_{\beta}(\omega)^2}\right] \approx \beta(\mathbf{x}_R,\omega). \tag{2.37}$$

Note that quality factors for P-wave and S-wave propagation are different. Typically, $Q_{\beta}(\omega) < Q_{\alpha}(\omega)$. Equations (2.36) and (2.3.7) demonstrate that co-incident observations of particle velocity, particle rotation, and displacement divergence may, in principle, be used to infer the frequency-dependent phase speeds of plane anelastic P- and S-waves at a single receiver point $\mathbf{x}_R$.

2.4 Summary

The primary goal of this section is to rigorously demonstrate that co-incident and contemporaneous recordings of the particle velocity vector, particle rotation vector, and displacement divergence scalar contain sufficient information to infer the type, direction, and speed of a seismic wave. We have established this for plane compressional and shear body waves propagating within homogeneous and isotropic elastic or anelastic media. Complications associated with anisotropic (i.e., direction dependent) media as well as interface or surface waves, where particle motion is no longer strictly longitudinal or transverse, are beyond the scope of this study. The inferences are approximately correct for spherical elastic waves, provided the receiver point resides within the far-field of the seismic energy source. This analysis provides justification for our assertion that all conclusions remain valid for *locally plane* body waves propagating within *locally homogeneous* media. Isolated, non-interfering plane waves of a single polarization (P or S) are also assumed. Either displacement divergence or particle rotation, or both, functions as an identifier of wave type. Determination of wave speeds for anelastic waves, where phase speeds are frequency-dependent, is approximate, although highly accurate, even for strongly attenuative (i.e., low Q) media. Finally, we demonstrate that co-located recordings of 3C particle velocity and

pressure are insufficient to determine P-wave speed. This provides a strong motivation for developing a displacement divergence sensor, or a more general displacement gradient sensor.

3.0 AZIMUTH SCANNING ALGORITHM

The development of the previous section demonstrates that co-located 3C translational and rotational seismometers provide, in principle, sufficient information to discern the type, direction, and speed of incident seismic waves. However, the particular mathematical formulae that are derived are not robust for use with actual seismic data. Forming a time-varying ratio of recorded trace data (as in equations (2.12), (2.13) for P-waves and (2.17), (2.18) for S-waves), is numerically unstable, and subject to large error when the traces are contaminated with noise. Moreover, the approach does not exploit the fact that the propagating seismic wavelet $w'(t)$ possesses extended time duration. In this section we develop rudimentary theory for more stable numerical algorithms for inferring incident wave direction and speed. The approach cross-correlates the recorded particle rotation and velocity vectors over a finite-length time window. The method utilizes the whole of the seismic wavelet, and thus should be less sensitive to ambient noise. The approach, referred to as an *azimuth scanning algorithm*, is first developed in the simplified context of horizontally-propagating SH waves, and then generalized to a three-dimensional situation.

3.1 Horizontal SH Wave Propagation

Begin by assuming horizontal SH plane wave propagation in the direction of unit vector **n**. Hence, propagation and polarization vectors are given by

$$\mathbf{n} = n_x \mathbf{e}_x + n_y \mathbf{e}_y = (\cos\theta_n)\mathbf{e}_x + (\sin\theta_n)\mathbf{e}_y, \tag{3.1a}$$

$$\mathbf{p} = p_x \mathbf{e}_x + p_y \mathbf{e}_y = (-\sin\theta_n)\mathbf{e}_x + (\cos\theta_n)\mathbf{e}_y, \tag{3.1b}$$

where θ_n is the azimuth angle, measured in the clockwise sense from the $+x$ axis ($0 \le \theta_n < 2\pi$). Clearly, $\|\mathbf{n}\| = \|\mathbf{p}\| = 1$ and $\mathbf{n}\cdot\mathbf{p} = 0$, as required. Also, the cross product $\mathbf{n}\times\mathbf{p} = (n_x p_y - n_y p_x)\mathbf{e}_z = \mathbf{e}_z$ points in the vertical ($+z$) direction, and thus is perpendicular to both **p** and **n**.

From equations (2.9) and (2.10), the particle velocity and particle rotation vectors observed at a receiver position $\mathbf{x}_R = (x_R, y_R, 0)$ are given by

$$\mathbf{v}(x_R, y_R, t) = U\left[(-\sin\theta_n)\mathbf{e}_x + (\cos\theta_n)\mathbf{e}_y\right] w'\left(t - \frac{x_R\cos\theta_n + y_R\sin\theta_n}{\beta}\right), \tag{3.2a}$$

$$\mathbf{r}(x_R, y_R, t) = -\frac{U}{\beta}\mathbf{e}_z\, w'\left(t - \frac{x_R\cos\theta_n + y_R\sin\theta_n}{\beta}\right). \tag{3.2b}$$

We assume that the incident wave is an S-wave, already identified as such by a non-zero particle rotation trigger. Azimuth angle θ_n is unknown, and is to be inferred from the measured seismic data. Hence, consider the horizontal particle velocity vector **v** resolved along a horizontal "candidate" polarization vector $\hat{\mathbf{p}}$ defined by

$$\hat{\mathbf{p}} = \left(-\sin\theta\right)\mathbf{e}_x + \left(\cos\theta\right)\mathbf{e}_y , \tag{3.3a}$$

with $0 \le \theta < 2\pi$. The vector dot product of **v** and $\hat{\mathbf{p}}$ is the scalar

$$\hat{v}\left(x_R, y_R, t\right) \equiv \hat{\mathbf{p}} \cdot \mathbf{v}\left(x_R, y_R, t\right) = U\left[\sin\theta\sin\theta_n + \cos\theta\cos\theta_n\right] w'\left(t - \frac{x_R\cos\theta_n + y_R\sin\theta_n}{\beta}\right). \tag{3.3b}$$

Now, cross-correlate the observed vertical rotation component with the candidate horizontal velocity component $\hat{v}$:

$$\Phi\left(\theta, t\right) \equiv r_z\left(x_R, y_R, t\right) \otimes \hat{v}\left(x_R, y_R, t\right) \equiv \int_{-\infty}^{+\infty} r_z\left(x_R, y_R, \tau\right)\hat{v}\left(x_R, y_R, \tau - t\right) d\tau$$

$$= -\frac{U^2}{\beta}\left(\sin\theta\sin\theta_n + \cos\theta\cos\theta_n\right) \times \int_{-\infty}^{+\infty} w'\left(\tau - \frac{x_R\cos\theta_n + y_R\sin\theta_n}{\beta}\right) w'\left(\tau - t - \frac{x_R\cos\theta_n + y_R\sin\theta_n}{\beta}\right) d\tau$$

$$= -\frac{U^2}{\beta}\cos\left(\theta - \theta_n\right) \mathrm{A}_{w'w'}\left(t\right), \tag{3.4}$$

where $\mathrm{A}_{w'w'}\left(t\right)$ is the (non-normalized) auto-correlation function of the particle velocity wavelet $w'(t)$. The cross-correlation $\Phi(\theta,t)$ is a trigonometric function of the candidate azimuth angle θ; the absolute value achieves its positive extremum at $\theta = \theta_n$ and negative extremum at $\theta = \theta_n + \pi$ (modulo 2π). This observation suggests an elementary *azimuth scanning algorithm* for determining the true angle of plane wave propagation at the receiver. Simply evaluate the cross-correlation objective function $\Phi(\theta,t)$ with the observed seismic data over the candidate angular range $0 \le \theta < 2\pi$, and retain the particular angle $\theta_{\max}$ that maximizes the zero-time lag value of $|\Phi(\theta,t)|$. This angle is taken as the best estimate of the true azimuth θ_n. In the language of applied mathematics, this algorithmic approach corresponds to a nonlinear optimization problem solved via a search method. The examples described in section 4.0 successfully apply this method to both synthetic and field-acquired seismic data. Moreover, as equation (3.4) indicates, the non-zero lag values of $\Phi(\theta,t)$ provide some information on the propagating seismic wavelet, in the form of the autocorrelation function where $\mathrm{A}_{w'w'}\left(t\right)$.

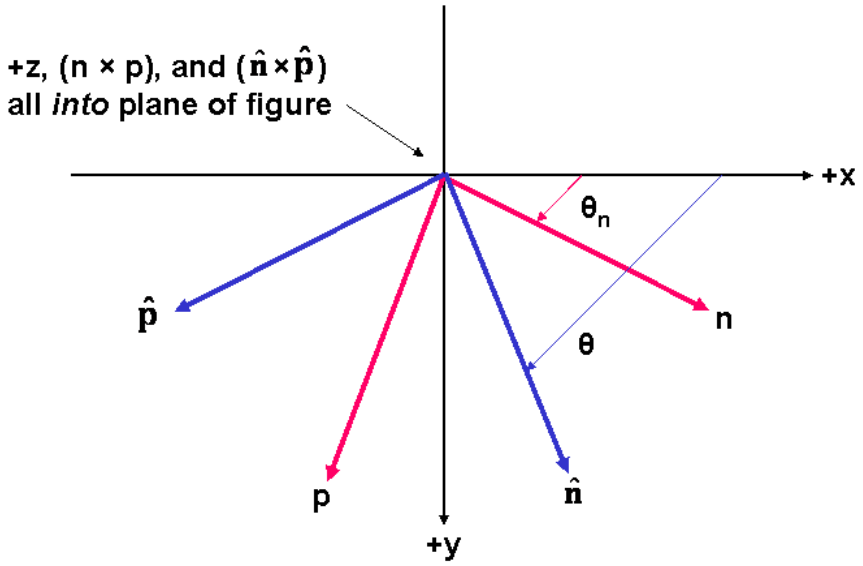

Figure 3.1. Plan view in horizontal (*xy*) plane of true propagation and polarization vectors (**red** arrows) and candidate propagation and polarization vectors (**blue** arrows). Azimuth angles θ_n and θ increase in the clockwise sense. Unit polarization vectors $\mathbf{p}$ and $\hat{\mathbf{p}}$ lead unit propagation vectors $\mathbf{n}$ and $\hat{\mathbf{n}}$ in azimuth by 90°, respectively.

3.2 Three-Dimensional Generalization

In the previous section, the incident plane shear wave was assumed to be i) horizontally-propagating, and ii) horizontally-polarized. Hence, the particle rotation vector is known to be *a priori* vertically-oriented (in the -*z*-direction). Determination of the incident propagation direction entails a simple one-dimensional search over the allowed 360° range of azimuth angle. However, if the restricting assumptions are relaxed, then a full three-dimensional search over *three* angles becomes necessary.

Let the unit vector describing the propagation direction of a plane wave in 3D space be

$$\mathbf{n} = \left(\cos\theta_n \sin\phi_n\right)\mathbf{e}_x + \left(\sin\theta_n \sin\phi_n\right)\mathbf{e}_y + \left(\cos\phi_n\right)\mathbf{e}_z , \tag{3.5a}$$

where $\theta_n \left(0 \le \theta_n < 2\pi\right)$ is the azimuth angle and $\phi_n \left(0 \le \phi_n < \pi\right)$ is the polar angle. A plane shear wave is polarized tranverse to this propagation direction. The unit polarization vector is given by

$$\begin{aligned}\mathbf{p} &= \cos\delta_n\left[\left(-\sin\theta_n\right)\mathbf{e}_x + \left(\cos\theta_n\right)\mathbf{e}_y\right], \\ &+ \sin\delta_n\left[\left(-\cos\theta_n \cos\phi_n\right)\mathbf{e}_x + \left(-\sin\theta_n \cos\phi_n\right)\mathbf{e}_y + \left(\sin\phi_n\right)\mathbf{e}_z\right].\end{aligned} \tag{3.5b}$$

It is easily demonstrated that $\|\mathbf{n}\| = \|\mathbf{p}\| = 1$ and $\mathbf{p}\cdot\mathbf{n} = 0$. Angle δ_n $(0 \le \delta_n \le \pi/2)$ measures the relative amount of SH or SV motion in the incident plane wave. $\delta_n = 0$ implies pure SH motion, whereas $\delta_n = \pi/2$ implies pure SV motion. For $0 < \delta_n < \pi/2$, the incident wave is a mixture, in varying proportions, of both

SH and SV motion (see Figure 3.2). For the case of horizontally-polarized SH motion, $\phi_n = \pi/2$ and $\delta_n = 0$, equations (3.5a,b) reduce to the previous expressions (3.1a,b).

In a manner similar to the previous section, "candidate" propagation and polarization vectors are now defined as

$$\hat{\mathbf{n}} = (\cos\theta \sin\phi)\mathbf{e}_x + (\sin\theta \sin\phi)\mathbf{e}_y + (\cos\phi)\mathbf{e}_z, \tag{3.6a}$$

and

$$\begin{aligned}\hat{\mathbf{p}} = \cos\delta\big[\,(-\sin\theta)\mathbf{e}_x + (\cos\theta)\mathbf{e}_y\,\big], \\ + \sin\delta\big[\,(-\cos\theta\cos\phi)\mathbf{e}_x + (-\sin\theta\cos\phi)\mathbf{e}_y + (\sin\phi)\mathbf{e}_z\,\big],\end{aligned} \tag{3.6b}$$

respectively, where θ and ϕ are candidate azimuth and polar propagation angles. The observed particle velocity vector (equation (2.9)) vector can be resolved along $\hat{\mathbf{p}}$, yielding the scalar analogue

$$\hat{v}(\mathbf{x}_R, t) \equiv \hat{\mathbf{p}} \cdot \mathbf{v}(\mathbf{x}_R, t) = U\,(\hat{\mathbf{p}} \cdot \mathbf{p})\, w'\left(t - \frac{\mathbf{x}_R \cdot \mathbf{n}}{\beta}\right). \tag{3.7}$$

As indicated by equation (2.10), the particle rotation vector is perpendicular to both **p** and **n**. Hence, define a unit vector $\mathbf{q} \equiv \mathbf{n} \times \mathbf{p}$. The components of this cross product are

$$\begin{aligned}\mathbf{q} = \mathbf{n} \times \mathbf{p} = &(\sin\delta_n \sin\theta_n - \cos\delta_n \cos\theta_n \cos\phi_n)\mathbf{e}_x \\ &-(\cos\delta_n \sin\theta_n \cos\phi_n + \sin\delta_n \cos\theta_n)\mathbf{e}_y \\ &+(\cos\delta_n \sin\phi_n)\mathbf{e}_z,\end{aligned} \tag{3.10}$$

from which it can be verified that $\mathbf{n} \cdot \mathbf{q} = \mathbf{p} \cdot \mathbf{q} = 0$, as required. Figure 3.2 indicates that **p** and **q** are contained in the plane perpendicular to the propagation direction **n**, and are orthogonal. Resolving the observed particle rotation vector (2.10) along a "candidate" $\hat{\mathbf{q}}$ unit vector gives the scalar

$$\hat{r}(\mathbf{x}_R, t) \equiv \hat{\mathbf{q}} \cdot \mathbf{r}(\mathbf{x}_R, t) = -\frac{U}{\beta}(\hat{\mathbf{q}} \cdot \mathbf{q})\; w'\left(t - \frac{\mathbf{x}_R \cdot \mathbf{n}}{\beta}\right). \tag{3.11}$$

Then, the cross-correlation function of the scalar particle velocity and rotation is

$$\Phi(\theta, \phi, \delta, t) \equiv \hat{r}(\mathbf{x}_R, t) \otimes \hat{v}(\mathbf{x}_R, t) \equiv \int_{-\infty}^{+\infty} \hat{r}(\mathbf{x}_R, \tau)\, \hat{v}(\mathbf{x}_R, \tau - t)\, d\tau$$

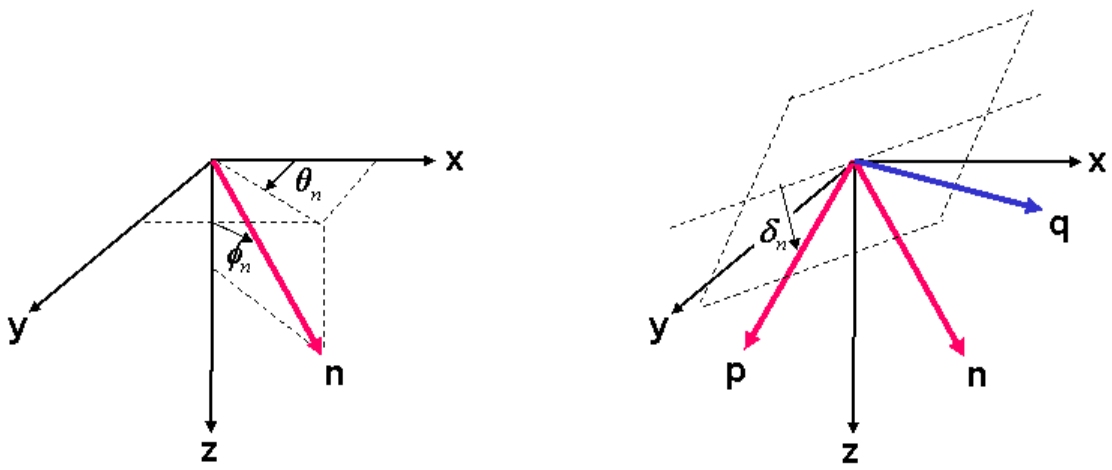

Figure 3.2. Orientations of the unit propagation direction vector **n** (left) and unit polarization vector **p** (right) for a plane shear wave propagating in three-dimensional (3D) space. The propagation vector is defined by azimuth angle θ_n and polar angle ϕ_n. The polarization vector **p** is contained in the plane normal to **n** (dashed outline), and has angle δ_n (measured in this plane) relative to the horizontal (xy) plane. Unit vector **q** (**blue** arrow) defines the positive direction of the particle rotation vector. **q** and **p** are co-planar and perpendicular to each other.

$$= -\frac{U^2}{\beta}(\hat{\mathbf{p}}\cdot\mathbf{p})(\hat{\mathbf{q}}\cdot\mathbf{q})\int_{-\infty}^{+\infty} w'\left(\tau - \frac{\mathbf{x}_R\cdot\mathbf{n}}{\beta}\right) w'\left(\tau - t - \frac{\mathbf{x}_R\cdot\mathbf{n}}{\beta}\right) d\tau$$

$$= -\frac{U^2}{\beta} f(\theta,\phi,\delta;\theta_n,\phi_n,\delta_n)\, A_{w'w'}(t), \tag{3.12}$$

where, once again, $A_{w'w'}(t)$ is the auto-correlation function of the underlying seismic wavelet $w'(t)$. Function f is defined by

$$f(\theta,\phi,\delta;\theta_n,\phi_n,\delta_n) \equiv (\hat{\mathbf{p}}\cdot\mathbf{p})(\hat{\mathbf{q}}\cdot\mathbf{q}) = \cos\psi_p \cos\psi_q, \tag{3.13}$$

and is a complicated trigonometric function of the six indicated angles. However, it is easy to understand that f is maximized when angle ψ_p (between $\hat{\mathbf{p}}$ and **p**) and angle ψ_q (between $\hat{\mathbf{q}}$ and **q**) each vanish. But this is precisely the condition that $\theta = \theta_n$, $\phi = \phi_n$, and $\delta = \delta_n$! In other words, the zero-time-lag value of the (absolute) cross-correlation objective function $|\Phi(\theta,\phi,\delta,t)|$ achieves its maximum when the candidate propagation and polarization vectors agree with the true vectors. A systematic search over the appropriate ranges of the *three* angles $\theta, \phi,$ and δ is now necessary to locate the maximum. Clearly, this entails greater computational effort than the simplified SH wave propagation situation described in the previous section.

3.3 Shear Wavespeed Determination

Equation (2.18) demonstrates that the ratio of particle velocity magnitude to particle rotation magnitude may be used to infer the shear wavespeed at a receiver $\mathbf{x}_R$. However, that approach is unstable with respect to ambient noise, and does not consider the whole of the seismic waveform $w'(t)$. Instead, consider the objective function

$$\Psi(\hat{\beta}) \equiv \text{norm}\left\{ \|\mathbf{v}(\mathbf{x}_R, t)\| - \hat{\beta}\|\mathbf{r}(\mathbf{x}_R, t)\| \right\}, \tag{3.14}$$

where $\hat{\beta}$ is a positive scalar, and norm $\{x\}$ is any suitable norm of quantity x. For example, the L_p norm of a function of time $x(t)$, defined over the time interval $[t_1, t_2]$, is

$$L_p[x] = \left\{ \frac{1}{t_2 - t_1} \int_{t_1}^{t_2} |x(t)|^p \, dt \right\}^{1/p}, \tag{3.15}$$

with $p > 0$. Time limits t_1 and t_2 should be selected to enclose the (common) waveform of the incident velocity and rotation vectors. From equations (2.9) and (2.10), the particular scalar $\hat{\beta}$ that minimizes the objective function $\Psi(\hat{\beta})$ is an estimate of the shear wavespeed at the receiver $\beta(\mathbf{x}_R)$. The one-dimensional search over $\hat{\beta}$ may be performed independently of the search for an optimum propagation direction $\mathbf{n}(\mathbf{x}_R)$, and does not involve any restricting assumptions about the spatial dimensionality (i.e., 2D or 3D) of wave propagation.

3.4 Frequency-Domain Effects

Another recurring question for this project has been "What is the influence of frequency-dependent transducer responses and data processing filters on the direction of wave propagation inferred by the azimuth scanning algorithm?" In this section, we conclude that the calculated direction is *not* affected, provided all such filtering operations are mathematically characterized as linear and time-invariant. We use the simple SH azimuth scanning approach of section 3.1 for analysis.

In order to investigate these issues, assume that the particle rotation and velocity vectors of the SH seismic wave incident at receiver location (x_R ,y_R) are modified by transducer measurement responses. Rotation and velocity sensors are considered linear and time-invariant transducers with impulse response functions $g_r(t)$ and $g_v(t)$, respectively. If each sensor generates an output voltage, then these impulse responses possess SI units $\text{V}/(\text{rad-s})$ and V/m, respectively. Transducer output voltages are then amplified, filtered, digitized, and recorded as unitless discrete samples by a seismic data recording system. However, we ignore the effects of recording instrument response. Alternately, if the recording system is also a linear and time-invariant device, its response can be mathematically amalgamated with the sensor responses.

After data acquisition, the recorded rotation and velocity time-series are subject to certain data processing operations, which we also characterize as linear and time-invariant filters with time-domain responses $f_r(t)$ and $f_v(t)$. Common operations are bandpass frequency filtering and transducer and/or recording instrument compensation. In contrast, multiplicative processes like windowing and gaining are linear and

time-variant filters, and are not considered here. Then, the processed particle rotation and velocity vectors are given by

$$\mathbf{r}_{\text{pro}}(x_R, y_R, t) \equiv \mathbf{r}(x_R, y_R, t) * g_r(t) * f_r(t), \tag{3.16a}$$

$$\mathbf{v}_{\text{pro}}(x_R, y_R, t) \equiv \mathbf{v}(x_R, y_R, t) * g_v(t) * f_v(t), \tag{3.16b}$$

where the asterisk denotes convolution with respect to time t. Resolving the processed particle velocity vector along a candidate horizontal unit polarization vector $\hat{\mathbf{p}} = (-\sin\theta)\mathbf{e}_x + (\cos\theta)\mathbf{e}_y$ gives the scalar

$$\hat{v}_{\text{pro}}(x_R, y_R, t) \equiv \hat{\mathbf{p}} \cdot \mathbf{v}_{\text{pro}}(x_R, y_R, t). \tag{3.17}$$

As described in section (3.1), we now cross-correlate the vertical component of the particle rotation with the candidate horizontal velocity. However, we now work with *processed* rotation and velocity vectors to obtain the θ-dependent objective function

$$\Phi_{\text{pro}}(\theta, t) \equiv r_{\text{pro-z}}(x_R, y_R, t) \otimes \hat{v}_{\text{pro}}(x_R, y_R, t). \tag{3.18}$$

Recall that symbol $\otimes$ denotes cross-correlation. Substituting expressions (3.16a) and (3.17), and utilizing well-known theorems of convolution and correlation mathematics, yields

$$\Phi_{\text{pro}}(\theta, t) = \Phi(\theta, t) * C_{g_r g_v}(t) * C_{f_r f_v}(t), \tag{3.19}$$

where two new cross-correlation functions are defined as

$$C_{g_r g_v}(t) \equiv g_r(t) \otimes g_v(t) = \int_{-\infty}^{+\infty} g_r(\tau) g_v(\tau - t)\, d\tau, \tag{3.20a}$$

$$C_{f_r f_v}(t) \equiv f_r(t) \otimes f_v(t) = \int_{-\infty}^{+\infty} f_r(\tau) f_v(\tau - t)\, d\tau. \tag{3.20b}$$

These cross-correlations are calculated between the two transducer responses, and the two post-acquisition processing filters. If rotation and velocity traces are subject to the same processing operations (e.g., identical bandpass frequency filters), then cross-correlation (3.20b) reduces to the auto-correlation $A_{ff}(t)$ of $f_r(t) = f_v(t) = f(t)$. Note that these cross-correlation functions do not depend on the azimuth angle θ of the candidate incident SH wave. Finally, substituting form (3.4) for the objective function $\Phi(\theta,t)$ gives

$$\Phi_{\text{pro}}(\theta, t) = -\frac{U^2}{\beta} \cos(\theta - \theta_n) \left[A_{w'w'}(t) * C_{g_r g_v}(t) * C_{f_r f_v}(t) \right]. \tag{3.21}$$

Hence, the objective function calculated from the recorded and processed data still achieves its maximum (for *any* fixed time lag), when the candidate propagation azimuth angle θ equals the true azimuth angle

θ_n! The effect of the transducer responses and processing filters is simply to corrupt (via convolutional smoothing) the auto-correlation function of the underlying propagating seismic wavelet $w'(t)$.

In order to understand frequency-dependent effects, Fourier transform equation (3.21) to the angular frequency domain. The Fourier transform of the objective function, denoted by a superposed tilde, is

$$\widetilde{\Phi}_{\text{pro}}(\theta,\omega) = -\frac{U^2}{\beta}\cos(\theta-\theta_n)\,\omega^2 W(\omega) W(\omega)^* G_r(\omega) G_v(\omega)^* F_r(\omega) F_v(\omega)^*, \tag{3.22}$$

where the asterisk-as-superscript on the right side indicates complex conjugation. The complex-valued Fourier transforms of transducer responses and processing filters are written in terms of frequency-dependent amplitude and phase spectra as

$$G_r(\omega) = |G_r(\omega)| \exp[+i\phi_r(\omega)], \qquad G_v(\omega) = |G_v(\omega)| \exp[+i\phi_v(\omega)],$$

$$F_r(\omega) = |F_r(\omega)| \exp[+i\varphi_r(\omega)], \qquad F_v(\omega) = |F_v(\omega)| \exp[+i\varphi_v(\omega)].$$

Then, equation (3.22) becomes

$$\widetilde{\Phi}_{\text{pro}}(\theta,\omega) = -\frac{U^2}{\beta}\cos(\theta-\theta_n)\,\omega^2 |W(\omega)|^2 |G_r(\omega)||G_v(\omega)||F_r(\omega)||F_v(\omega)|$$

$$\times \exp\{+i[\phi_r(\omega) - \phi_v(\omega) + \varphi_r(\omega) - \varphi_v(\omega)]\}. \tag{3.23}$$

Clearly, there is complicated dependence on frequency. Nevertheless, the amplitude of $\widetilde{\Phi}_{\text{pro}}$ achieves a maximum, for any frequency, when candidate and true propagation azimuth angles agree.

4.0 SYNTHETIC SEISMIC DATA EXAMPLE

4.1 Numerical Algorithm

In this section, we investigate the point seismic array concept with synthetic data calculated for a one-dimensional (1D) layered earth model representing a field site near Yucca Mountain, Nevada. Seismic data are generated with a numerical algorithm appropriate for three-dimensional (3D) wave propagation within an isotropic elastic medium. This algorithm solves a set of nine, coupled, first-order, partial differential equations called the *velocity-stress system* via an explicit, time-domain, finite-difference (FD) technique. The nine wavefield variables are the three orthogonal components of the particle velocity vector $v_i(\mathbf{x},t)$ (i = 1,2,3) and the six independent elements of the symmetric stress tensor $\sigma_{ij}(\mathbf{x},t)$ (i, j = 1,2,3 with $\sigma_{ij} = \sigma_{ji}$). Temporal and spatial FD operators have 2nd-order and 4th-order accuracy in the respective grid intervals, and are defined on staggered time-space grids. The algorithm generates all relevant seismological arrivals (P-waves, S-waves, reflections, refractions, mode-conversions, multiples, surface waves, interface waves, diffracted and scattered arrivals, etc.) with fidelity, provided temporal and spatial gridding intervals are sufficiently fine.

A technical description of the 3D FD elastic wave propagation algorithm, with particular reference to numerical accuracy issues, is given by Aldridge and Haney (2008).

For the purposes of this project, the primary modification to the seismic wave propagation algorithm (named ELASTI) involved implementing particle rotation receivers. First, define the *rotation rate vector* **w** as the **curl** of the particle velocity vector **v**:

$$\mathbf{w}(\mathbf{x},t) \equiv \mathbf{curl}\ \mathbf{v}(\mathbf{x},t). \tag{4.1a}$$

From equation (2.1), the rotation rate vector is the time derivative of the particle rotation vector **r**:

$$\mathbf{w}(\mathbf{x},t) = \frac{\partial \mathbf{r}(\mathbf{x},t)}{\partial t}. \tag{4.1b}$$

Thus, the three components of the rotation rate vector are obtained by taking time derivatives of equations (2.2a, b, and c). At a designated receiver location $\mathbf{x}_R$, the space partial derivatives in these expressions are approximated with centered discrete spatial differences of the three particle velocity components. Fourth-order accurate differencing is used, compatible with the FD accuracy used to propagate the elastic wavefield through the 3D spatial grid.

After the components of the particle rotation rate vector are calculated and stored for a specified receiver position, they may be integrated in time with a suitable numerical quadrature method to obtain the rotation components. However, for this project, we decided to work directly with calculated rotation rate seismograms. The particular rotational seismometer used for our field data acquisition experiments (the Entec Model R1, an electrochemical transducer) generates an output voltage proportional to input rotation rate (in radians/second). Also, it is our impression that other rotational motion transducers are sensitive to rotation rate, rather than the absolute rotation angle associated with seismic ground motion.

4.2 Layered Earth Model

The 1D earth model used for seismic wave propagation simulations represents the shallow subsurface geological/geophysical properties of a site near Yucca Mountain, Nevada. The model consists of six homogeneous and isotropic elastic layers overlying a halfspace. Numerical values of layer thickness h, P-wave speed V_P, S-wave speed V_S, and mass density ρ are given in the following table:

layer #	h (m)	V_P (m/s)	V_S (m/s)	ρ (kg/m^3)
1	4.0	697.8	351.5	1593
2	7.0	1715.7	990.6	1995
3	8.5	1161.6	670.5	1810
4	48.8	1583.7	914.4	1956
5	61.0	1689.5	975.4	1987
6	137.2	1742.2	1005.8	2003
7	∞	2428.3	1402.1	2176

Vertical profiles of the parameters are illustrated in Figure 4.1. These profiles exhibit some rather unusual structure, particularly in the shallowest portion of the model. The layer immediately below the surface has extremely low seismic wavespeeds, indicative of a loosely-consolidated and aerated desert sand or soil. Next, there is a high-velocity lid (layer #2, caliche?) overlying a low-velocity zone (layer #3). These are followed by a normal sequence of layers with increasing wavespeeds and mass density with depth. At 266.5 m, there is a sharp discontinuous increase in all medium parameters, perhaps representing the transition to well-consolidated bedrock.

The P-wave speed model was originally inferred from seismic refraction traveltime measurements obtained at this site. The S-wave speed model is constructed by assuming a Poisson ratio of $\sigma = 0.25$ for layers #2 through #7, a value considered typical for sedimentary rocks. The shallowest layer is assigned a larger Poisson ratio $\sigma = 0.33$. Shear wave speed is then obtained from compressional wave speed via

$$\frac{V_S}{V_P} = \left[\frac{1-2\sigma}{2(1-\sigma)} \right]^{1/2} .$$

$\sigma = 0.25$ implies the well-known wavespeed ration $V_S/V_P = 1/\sqrt{3} \approx 0.577$.

Mass density for each layer is obtained by assuming a "Gardner-style" relation

$$\frac{\rho}{\rho_{ref}} = \left(\frac{V_P}{V_{P-ref}} \right)^n ,$$

where n is an exponent. Note that $\rho = \rho_{ref}$ when $V_P = V_{P\text{-}ref}$. Re-arranging this expression gives

$$\rho = g\, V_P^n ,$$

where the proportionality factor $g = \rho_{ref} \big/ V_{P-ref}^{n}$ has the proper SI units $(kg/m^3)/(m/s)^n$ for conversion of wavespeed to mass density. Taking g = 310 (with V_P in m/s) and n = 0.25 (see Sheriff, 2002, page 157) yields the vertical density profile depicted in Figure 4.1 (right panel). The calculated density of the basement rock (layer #7) is quite reasonable for a consolidated sandstone.

A 3D gridded representation of the above 1D layered earth model is required for use in our finite-difference elastic wave propagation algorithm ELASTI. Earth model construction software LAYRS_1D sampled the vertical parameter profiles of V_P, V_S, and ρ on a uniformly-spaced, 3D rectangular grid defined by

$$\begin{aligned}(x_{\min}, \Delta x, N_x) &= (-60\ \text{m},\ 1\ \text{m}, 301),\\ (y_{\min}, \Delta y, N_y) &= (-150\ \text{m}, 1\ \text{m}, 301),\\ (z_{\min}, \Delta z, N_z) &= (-2\ \text{m}, 1\ \text{m}, 403).\end{aligned}$$

Thus, the total number of spatial gridpoints in this model is $N_x\, N_y\, N_z$ = 36,512,203. The minimum vertical coordinate $z_{\min}$ = –2 m is required to implement a stress-free surface at z = 0 m, which mimics seismic conditions at the air/earth interface.

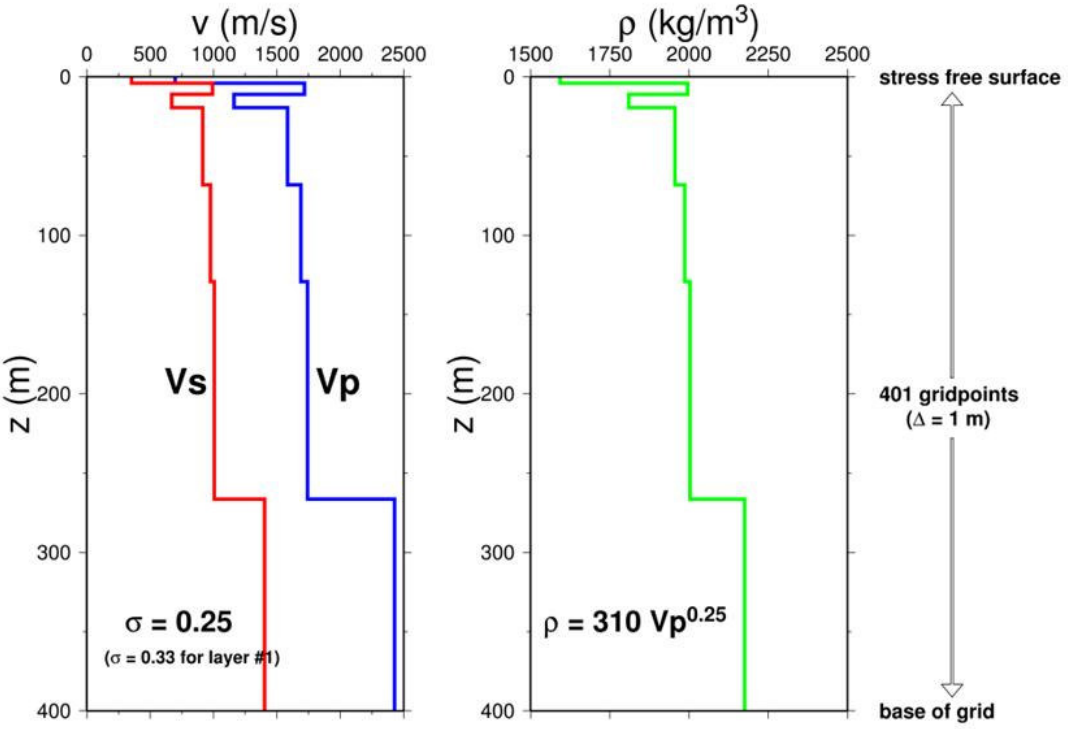

Figure 4.1. One-dimensional vertical profiles of P-wave and S-wave speeds (left panel) and mass density (right panel) representing seismic properties at the Yucca Mountain field data acquisition site. Shear wave speed V_S is constructed from compressional wave speed V_P by assuming a Poisson ratio σ for each (homogeneous and isotropic) elastic layer. Mass density ρ is obtained from an assumed "Gardner relation" dependence on V_P. Note the velocity/density reversal in the shallow subsurface, and the sharp increase in medium properties at depth ~267 m below the stress-free surface at z = 0 m.

4.3 Data Acquisition Configuration

The simulated recording geometry is designed to represent an actual source-receiver deployment used at the Yucca Mountain site, described in Section 5.0. Thus, there are six receiver stations arrayed on the stress-free surface at horizontal distances of 30 m, 59 m, 89 m, 118 m, 148 m, and 178 m from the source. Hence, the receiver station interval is approximately 30 m. As illustrated in Figure 4.2, each station is occupied by a so-called *seven component sensor*, consisting of a triaxial accelerometer, a triaxial rotation rate transducer, and a pressure sensor.

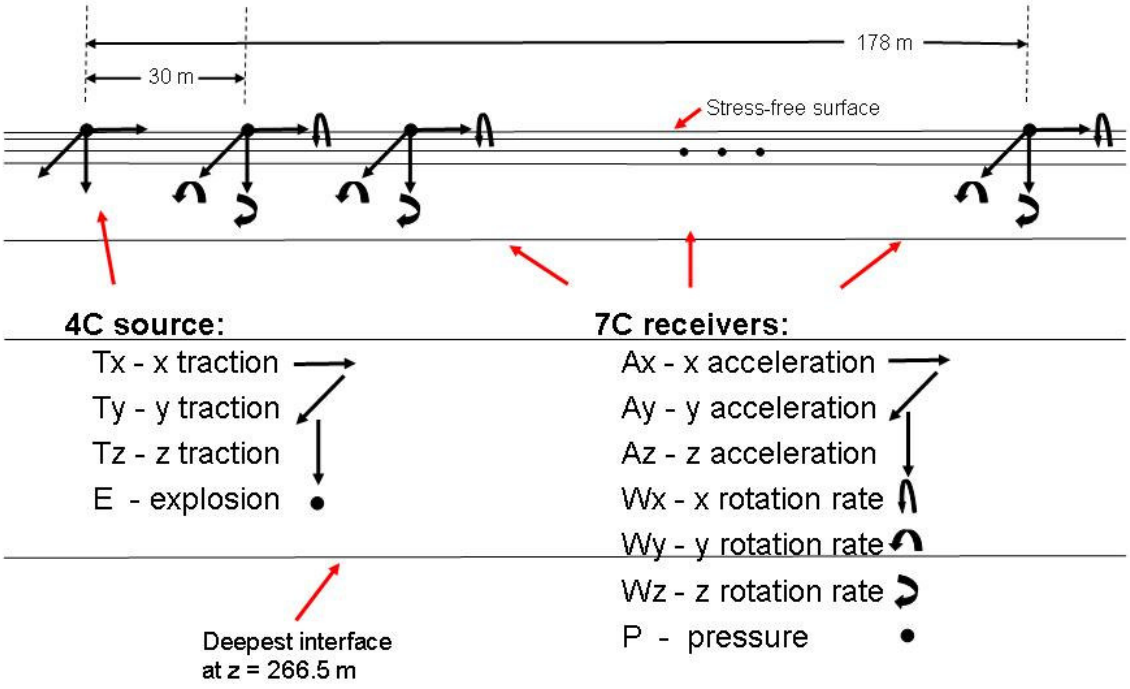

Figure 4.2. Data acquisition configuration used for computational modeling of seismic responses at the Yucca Mountain site. There are six receiver stations located on the horizontal stress-free surface, ranging from 30 m to 178 m in offset distance from the seismic energy source. Each receiver station is occupied by a seven component seismic sensor. Seismic sources consist of a three-component traction applied to the surface, and a shallow-buried explosion. Light horizontal lines indicate interfaces between homogeneous layers of the 1D elastic earth model.

Various point seismic energy sources are activated on, or immediately below, the surface of the model at horizontal coordinates $(x_S, y_S) = (0,0)$ m. Thus, a three-component (3C) time-varying traction is applied directly to the surface, in the inline ($+x$), crossline ($+y$), and vertical ($+z$) coordinate directions. This source is designed to replicate the physics of a 3C vibrator used for actual field data acquisition at the Yucca Mountain site (see Figure 5.1). Additionally, we conducted several seismic wave propagation simulations using an isotropic explosion buried 0.5 m (or one-half grid interval) beneath the surface, as well as a 3C body force vector at the same depth.

4.4 Computational Modeling Issues

Synthetic seismic data were calculated by the FD algorithm on the discrete time raster

$$\left(t_{\min}, \Delta t, N_t\right) = \left(0\text{ s},\ 0.000200\text{ s}, 10{,}001\right).$$

Thus, the duration of the seismic traces is 2.000 s. The FD timestep Δt = 0.2 ms equals ~98.2% of the maximum allowed timestep imposed by the Courant-Fredrichs-Lewy numerical stability condition:

$$\Delta t \le \Delta t_{CFL} = \frac{6}{7\sqrt{3}} \frac{\Delta h}{V_{\max}} \approx 0.495 \frac{\Delta h}{V_{\max}},$$

(Aldridge and Haney, 2006) where Δh is the spatial grid interval (assumed equal in all three coordinate directions) and V_{max} is the maximum wavespeed within the model.

The source waveform used for the numerical modeling is a discrete approximation to the temporal Dirac delta function $\delta(t)$ centered at time t = 0 s (= $t_{\min}$). Hence, calculated traces are properly referred to as "unit impulse response seismograms". The broadband nature of this impulsive source wavelet implies that the calculated responses will suffer severe numerical dispersion. Realistic seismograms are readily obtained by convolving the calculated impulse responses with a preferred source wavelet. For this study, our source wavelet is a *Ricker wavelet* characterized by a peak frequency f_p:

$$r(t) = \left[1 - 2\left(\pi f_p t\right)^2\right] \exp\left[-\left(\pi f_p t\right)^2\right].$$

A Ricker wavelet is zero-phase, and hence acausal. Thus, it is not a particularly realistic representation of the waveform of an explosion or surface impact. For these situations, a causal pulse like the Berlage wavelet (Aldridge, 1992) should be used. However, the Ricker waveform may a reasonable approximation to the autocorrelation function of a swept-frequency signal generated by a vibratory seismic energy source, as was used at the Yucca Mountain site. The frequency amplitude spectrum of the Ricker wavelet is given by

$$R(f) = \left[\frac{2}{\sqrt{\pi} f_p}\right] \left(\frac{f}{f_p}\right)^2 \exp\left[-\left(\frac{f}{f_p}\right)^2\right],$$

which has a maximum at $f = f_p$.

Care should be employed in choosing the peak frequency of the Ricker waveform used to convolve with the impulse response seismograms. The minimum wavelength propagating through the 3D grid is

$$\lambda_{\min} = \frac{V_{\min}}{f_{\max}},$$

where $V_{\min}$ is the minimum wavespeed in the earth model, and $f_{\max}$ is the maximum frequency. Normalizing by the spatial grid interval, and choosing $\lambda_{\min} / \Delta h \approx 5$ to minimize numerical dispersion effects (Aldridge and Haney, 2008) yields

$$f_{\max} = \frac{V_{\min}}{5\Delta h} = \frac{351.5 \text{ m/s}}{5 \text{ m}} \approx 70.3 \text{ Hz}.$$

How should the peak frequency of the convolving Ricker wavelet be chosen, so that this maximum frequency limit is honored? As indicated by Aldridge (2000), the *far-field* seismic wavelet radiated from a point force source in a homogeneous elastic wholespace is the first derivative of the source pulse. Thus, the far-field frequency spectrum of a Ricker source wavelet is $(i2\pi f)R(f)$. If we adopt the 1% level of the far-field frequency amplitude spectrum as the highest frequency propagating through the 3D grid, then the largest allowed peak frequency of the Ricker force source wavelet is

$$f_p\Big|_{\text{maximum}} = 23.75 \text{ Hz}.$$

We take this limit to hold for surface traction sources as well. The maximum allowed peak frequency for a body moment source (like an explosion) is slightly lower. The far-field seismic wavelet of a point explosion source activated in a homogeneous elastic wholespace equals the *second* derivative of the source wavelet, implying that its spectrum is $(i2\pi f)^2 R(f)$. Hence, again choosing the 1% level of the far-field spectrum as the upper frequency cutoff point, we obtain the largest allowed peak frequency of a Ricker moment source wavelet as

$$f_p\Big|_{\text{maximum}} = 22.50 \text{ Hz}.$$

For the bulk of the synthetic seismic data displayed in the following section, we used a convolving Ricker wavelet with a peak frequency f_p = 20 Hz, which is adequately below the above-stated limits. Thus, these data do not contain any adverse numerical dispersion artifacts. However, we have generated some data by convolving with Ricker wavelets with peak frequencies of 30 Hz and 40 Hz. The higher frequency components of these particular data are less well-resolved by the 1 m spatial grid interval, and hence may suffer numerical dispersion. Nevertheless, plots of these data appear reasonable. There are two potential reasons why numerical dispersion may be less than expected:

1) Much spectral energy of the propagating seismic pulse resides well below the upper cutoff point (i.e., the 1% level of the frequency amplitude spectrum). These Fourier components have longer seismic wavelengths and are well-sampled by the 1 m spatial grid interval.
2) The very low velocity media in the earth model is restricted to a relatively small portion (i.e., the thin layer #1) of the total model. Seismic waves propagating in the higher velocity layers have longer wavelengths, and are also sampled more finely by the 1 m grid interval.

Rigorous justification for the common "five grid intervals per shortest propagating wavelength" rule-of-thumb is provided by Aldridge and Haney (2008). At this spatial sampling rate, the numerical phase speed differs from the true wavespeed of the underlying continuum by less than ~1%.

The primary advantage associated with calculating impulse response seismograms pertains to flexibility. Impulse response seismograms are calculated with a *single* execution of the FD algorithm. Then, seismograms for a variety of different source wavelets are easily obtained via post-simulation convolution. There is no need to execute the FD algorithm repeatedly with each source pulse..

4.5 Synthetic Data Examples

The following figures illustrate synthetic seismic data calculated for the 1D layered Yucca Mountain site earth model. Three-component particle *acceleration* and particle *rotation rate* traces are displayed. Although the theory underlying the point seismic array concept outlined in previous sections utilized particle velocity and particle rotation data, the same results hold if both data types are differentiated with respect to time. Moreover, as indicated previously, current generation rotational motion transducers appear to be sensitive to rotation rate.

Figure 4.3 and 4.4 depict the 3C acceleration and rotation rate traces recorded at the six surface receiver stations, when a vertical traction (T_z) is applied to the stress-free surface at the source point. The convolving wavelet is Ricker wavelet with peak frequency f_p = 20 Hz. No time- or offset-dependent display gain is applied. The plot amplitude level is identical for each panel within a figure, so relative trace amplitudes can be directly compared. With a vertically-oriented source, the *y*-component of acceleration and the *x*- and *z*-components of the rotation rate vanish. Thus, orthogonality condition (2.21) is numerically verified under earth model and wave propagation circumstances that are considerably more complicated than originally anticipated! [Recall that expression (2.21) is derived under the assumption of spherical wave propagation from a point body source within a homogeneous elastic wholespace.]

The outstanding feature of the seismic data depicted in Figures 4.3 and 4.4 is a strongly-dispersed surface wave train propagating slowly across the receiver spread. These surface waves, with an appearance similar to resonant oscillations, result from the unusual velocity structure of the 1D Yucca Mountain site earth model of Figure 4.1. Interestingly, if a seismic energy source wavelet with lower spectral content is used, then resonant behavior disappears. Figures 4.5 and 4.6 display the analogous traces obtained with a convolving Ricker wavelet with peak frequency f_p = 10 Hz (i.e. half of that used for Figures 4.3 and 4.4). Surface wave amplitudes are strongly attenuated, and the reflected arrival from the basement interface is clearly discernable on the *z*-component acceleration record between 400 ms and 600 ms. The traces obtained by doubling the convolving Ricker pulse peak frequency to f_p = 40 Hz are displayed in Figures 4.7 and 4.8. The resonant behavior returns, although with diminished amplitude. The influence of the spectral content of the seismic energy source on recorded data is obvious. [We emphasize (again) that all of these data were calculated with a *single* execution of the FD wave propagation algorithm.]

Synthetic data generated by a horizontal surface traction, oriented in the crossline (+*y*) direction are illustrated in Figures 4.9 and 4.10. A 20 Hz convolving Ricker wavelet is used to generate these traces, so numerically-induced dispersion is minimal. In contrast with the earlier situation, acceleration now appears on the *y*-component, and rotation rate appears on the *x*- and *z*-components. Nevertheless, the orthogonality condition (2.21) still holds. This high-amplitude surface wave train, consisting of SH rectilinear motion, propagates faster than the resonant oscillations displayed in Figure 4.3. An unanticipated result is the appearance of low-amplitude rotational motion on the inline horizontal (+*x*) component.

Traces obtained from an inline (T_x) surface traction source are displayed in Figure 4.11 and 4.12, again with a 20 Hz peak frequency convolving Ricker wavelet. Waveforms and amplitudes differ from the rectilinear SV motion generated by the vertical (T_z) traction source (Figures 4.3 and 4.4). In particular, the coda of the *x*-component acceleration appears much less coherent. Finally, acceleration and rotation rate traces generated by a shallow isotropic explosion (Figures 4.13 and 4.14) are similar to those created by a vertical surface traction (Figures 4.3 and 4.4). Frequency content is nearly identical, because there is little difference in the far-field bandwidth of the traction source (3.2-59.2 Hz) and explosion source (5.5-62.5 Hz) frequency spectra. However, amplitudes differ by about an order of magnitude.

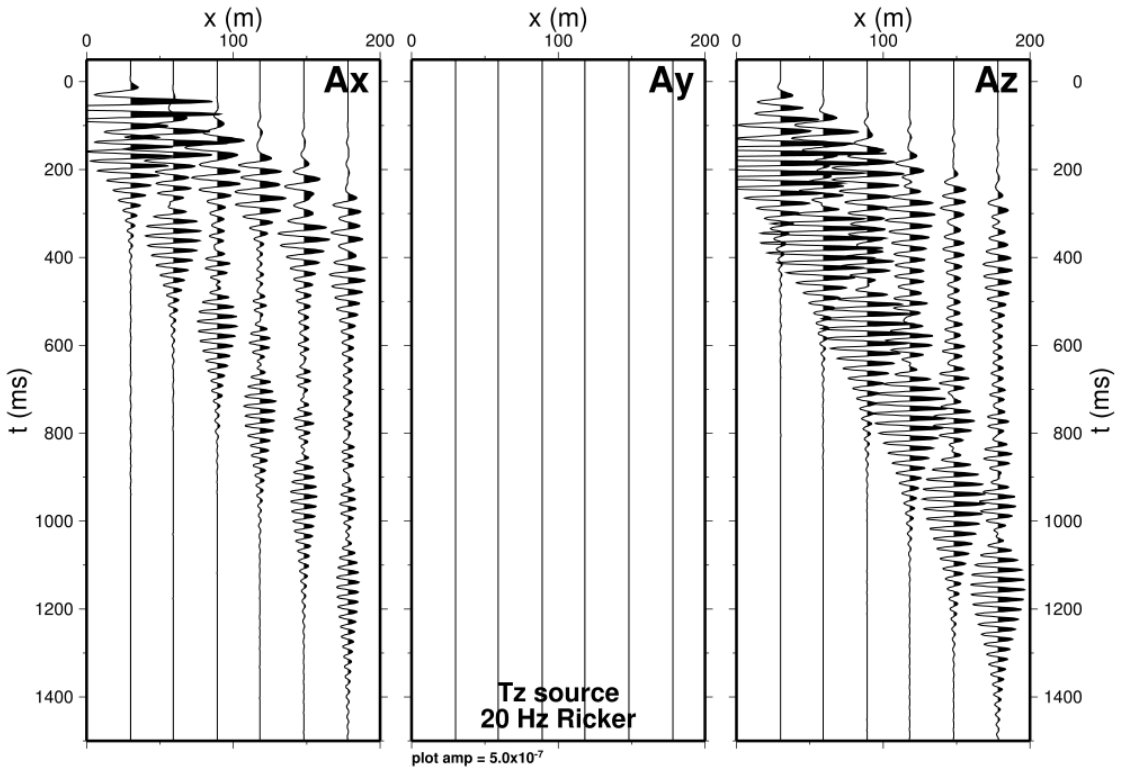

Figure 4.3. 3C particle acceleration traces generated by a vertical (T_z) surface traction source activated by a 20 Hz Ricker wavelet.

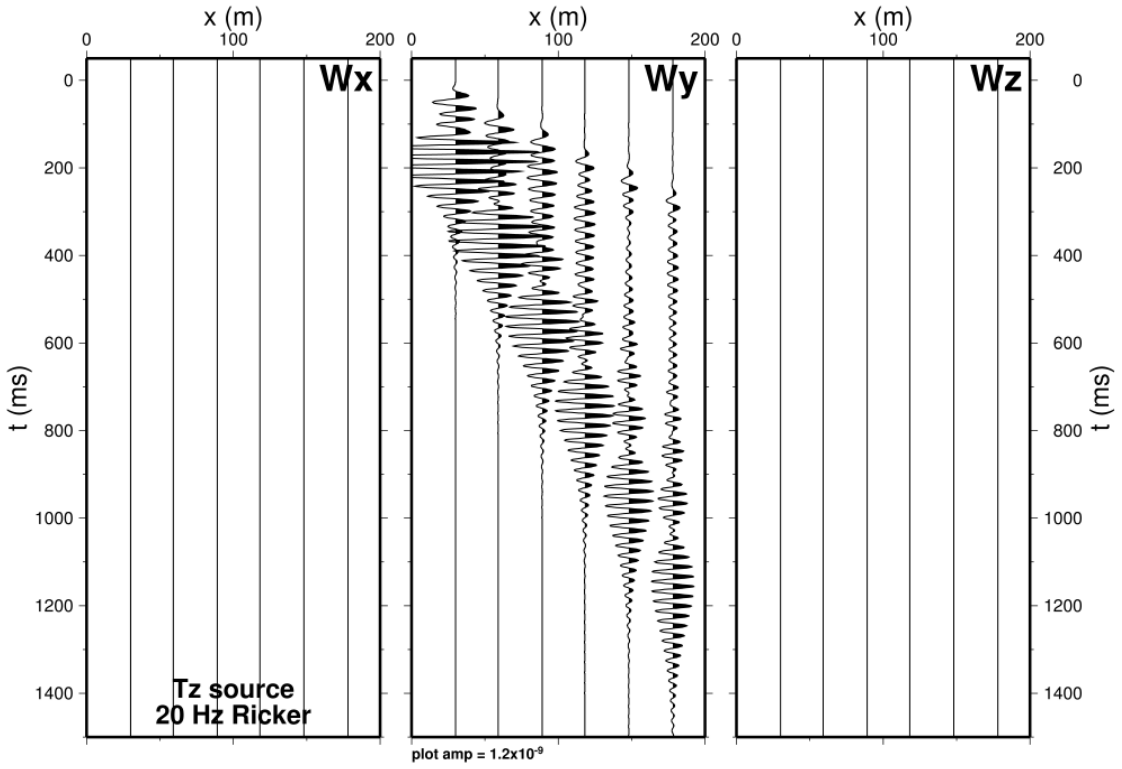

Figure 4.4. 3C particle rotation rate traces generated by a vertical (T_z) surface traction source activated by a 20 Hz Ricker wavelet.

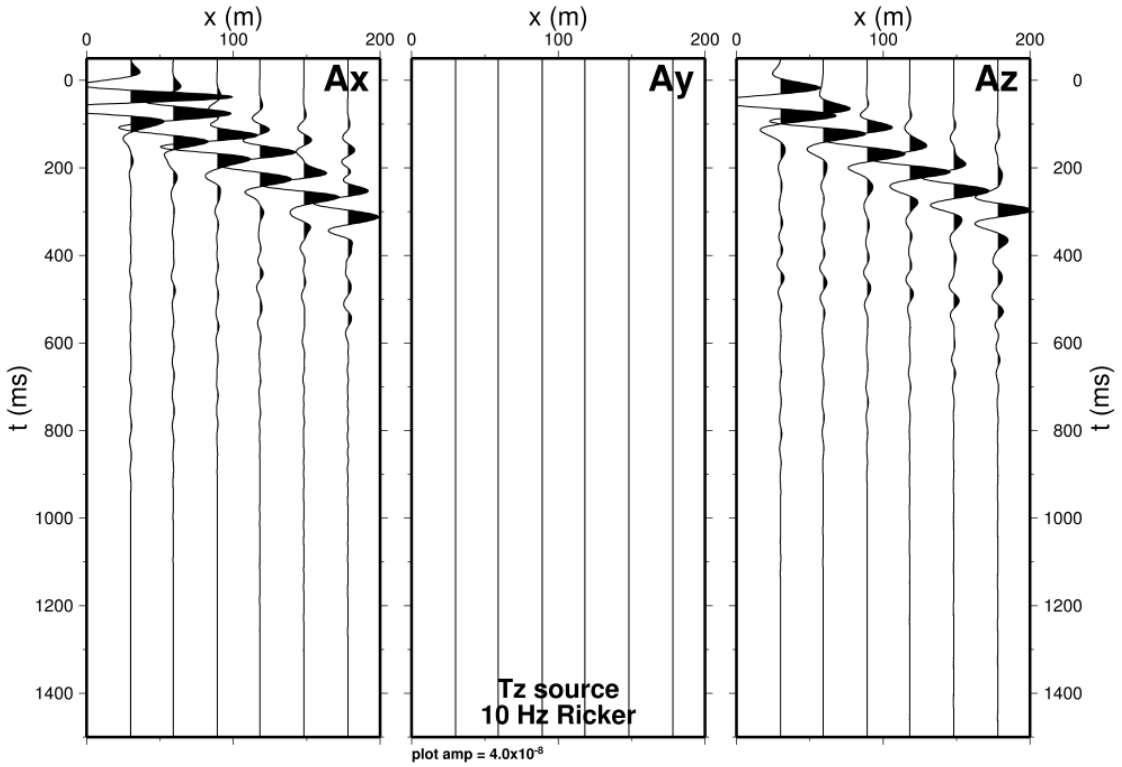

Figure 4.5. 3C particle acceleration traces generated by a vertical (T_z) surface traction source activated by a 10 Hz Ricker wavelet.

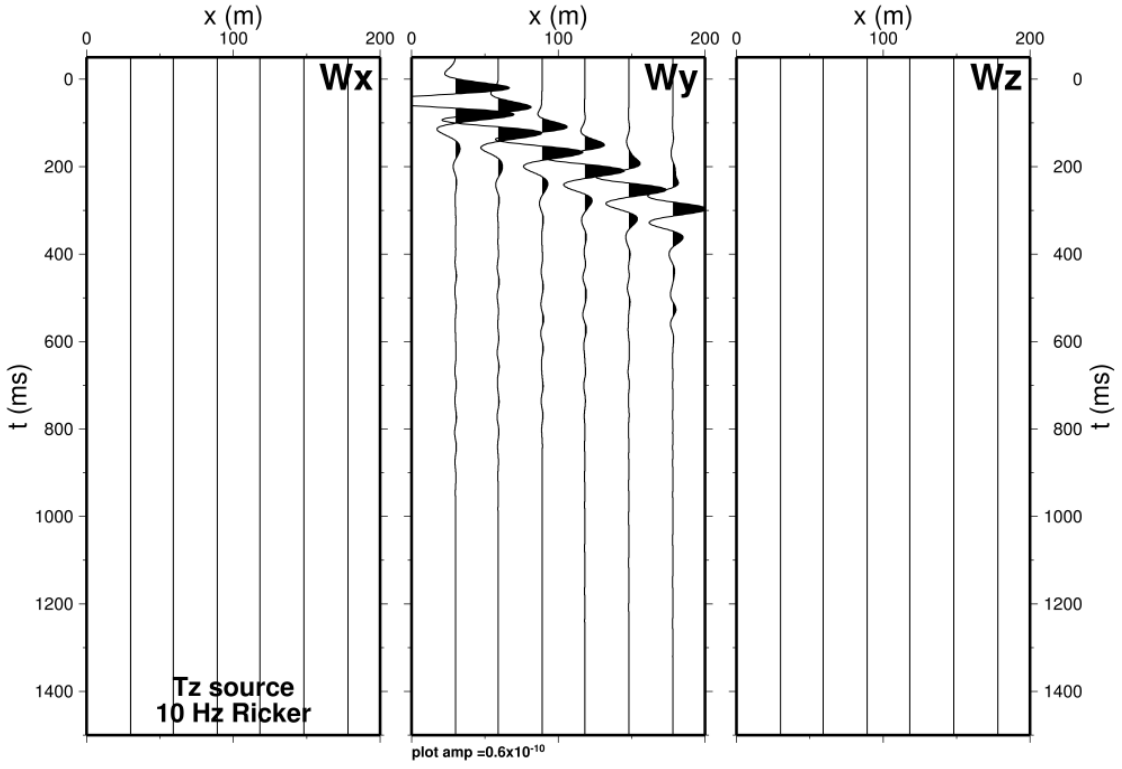

Figure 4.6. 3C particle rotation rate traces generated by a vertical (T_z) surface traction source activated by a 10 Hz Ricker wavelet.

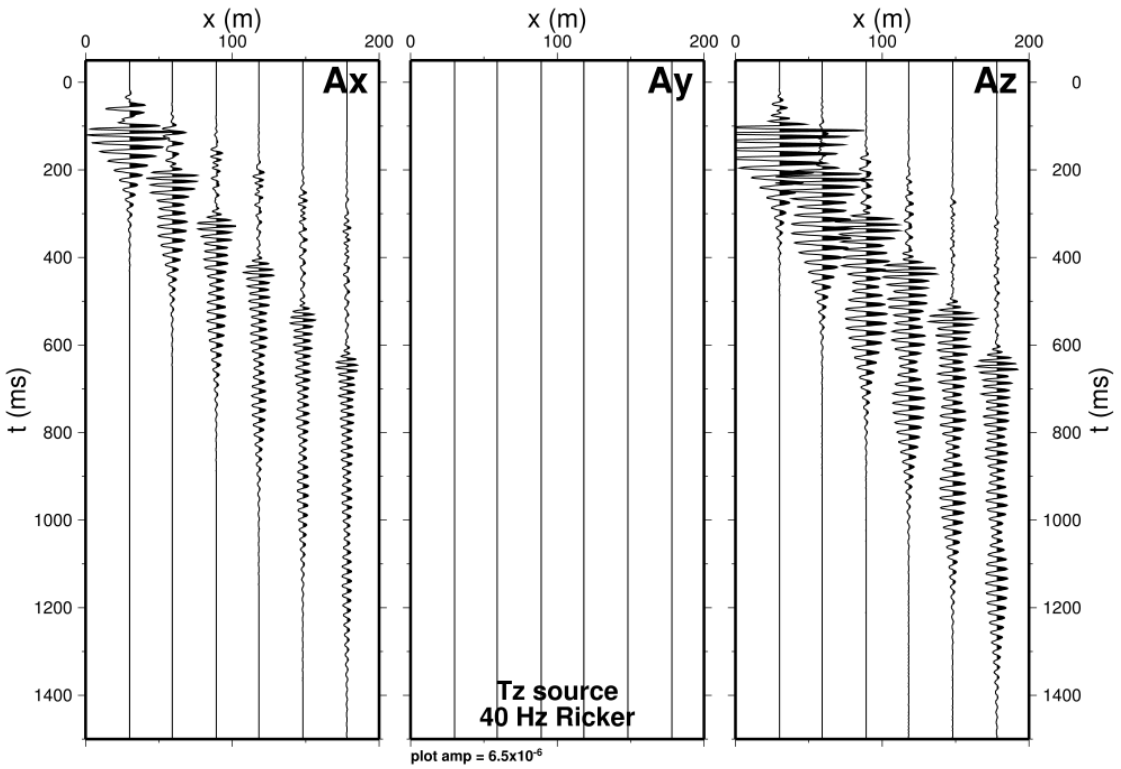

Figure 4.7. 3C particle acceleration traces generated by a vertical (T_z) surface traction source activated by a 40 Hz Ricker wavelet.

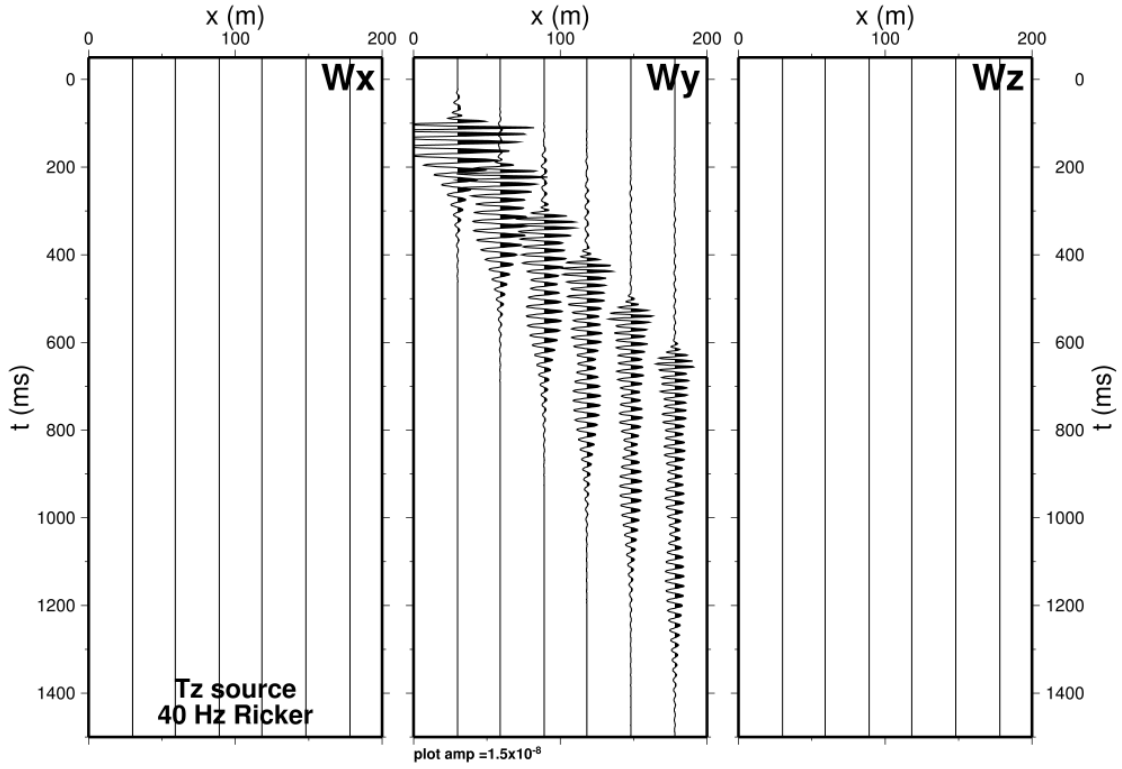

Figure 4.8. 3C particle rotation rate traces generated by a vertical (T_z) surface traction source activated by a 40 Hz Ricker wavelet.

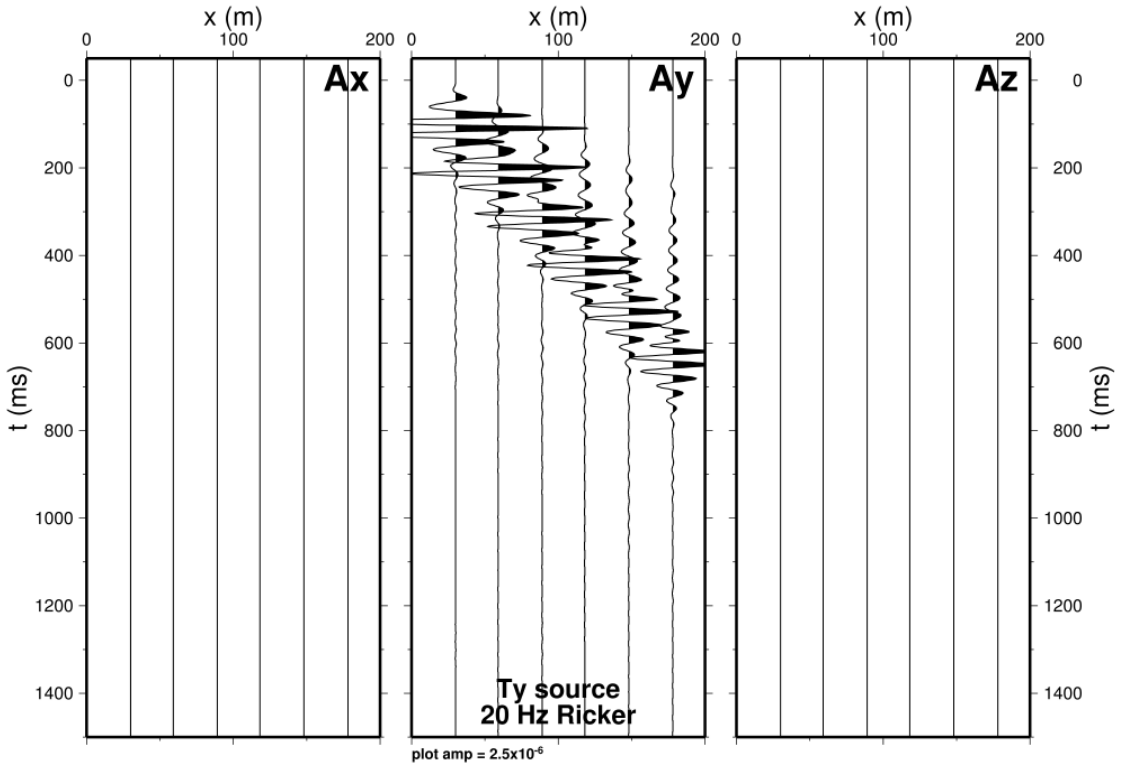

Figure 4.9. 3C particle acceleration traces generated by a crossline horizontal (T_y) surface traction source activated by a 20 Hz Ricker wavelet.

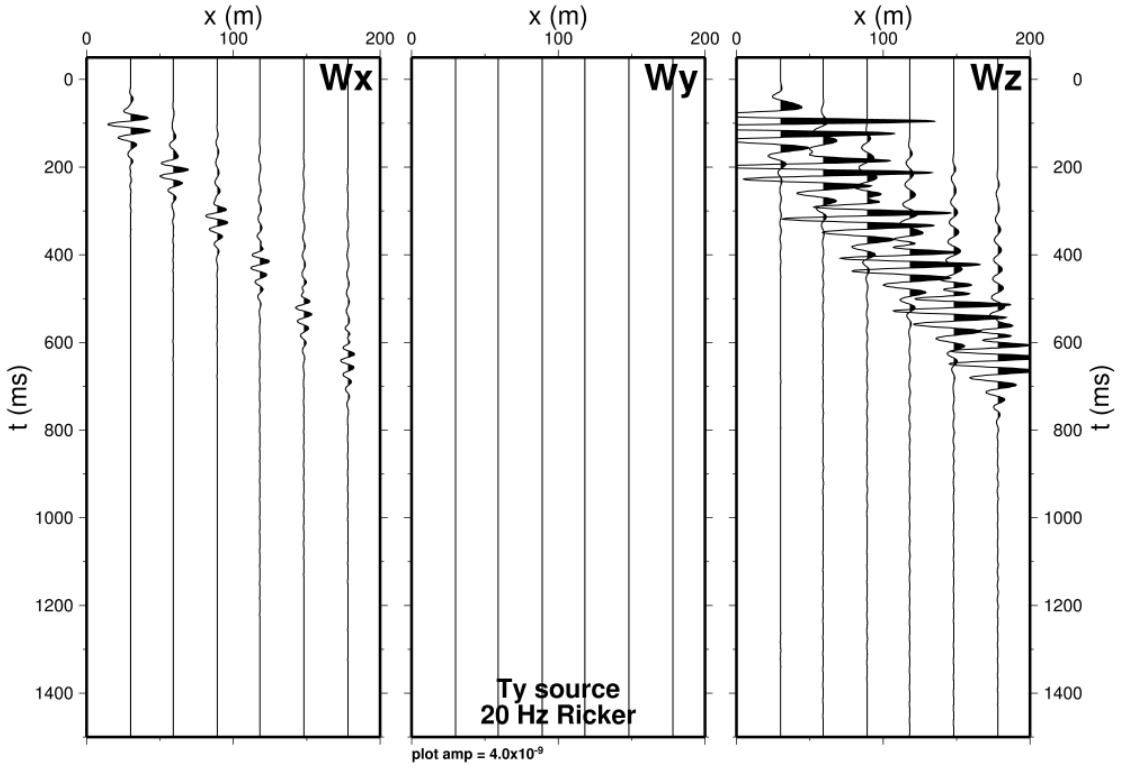

Figure 4.10. 3C particle rotation rate traces generated by a crossline horizontal (T_y) surface traction source activated by a 20 Hz Ricker wavelet.

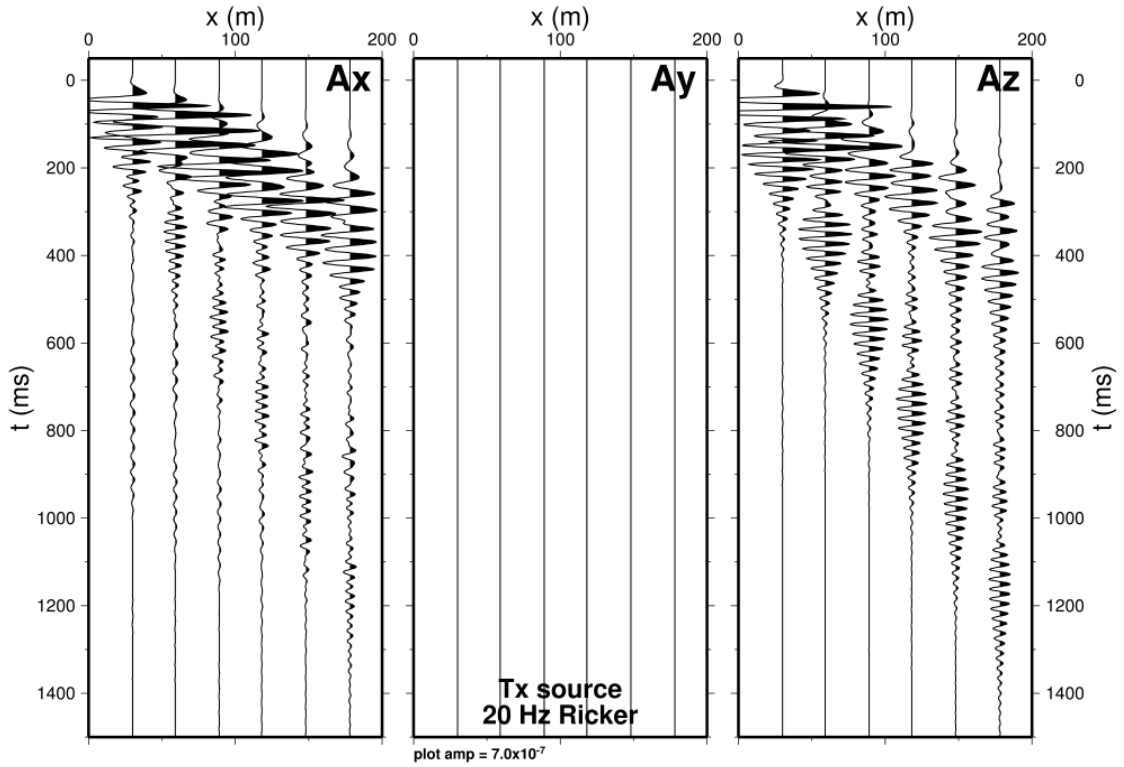

Figure 4.11. 3C particle acceleration traces generated by a inline horizontal (T_x) surface traction source activated by a 20 Hz Ricker wavelet.

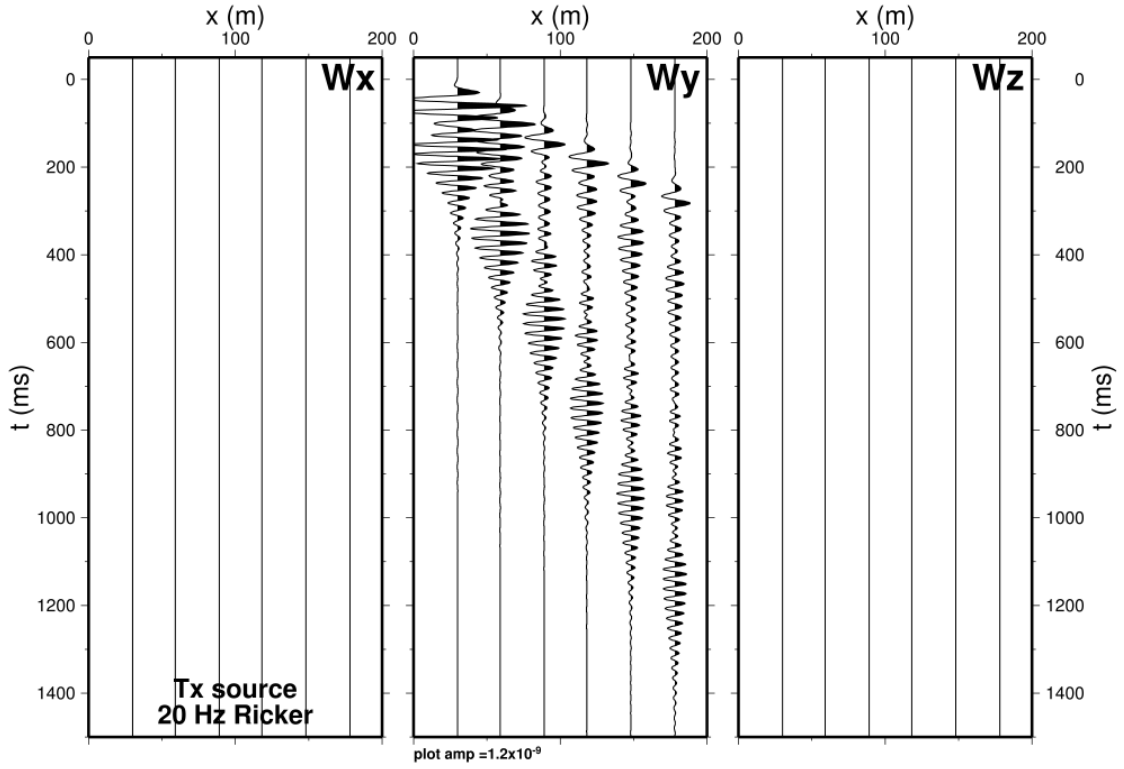

Figure 4.12. 3C particle rotation rate traces generated by a inline horizontal (T_x) surface traction source activated by a 20 Hz Ricker wavelet.

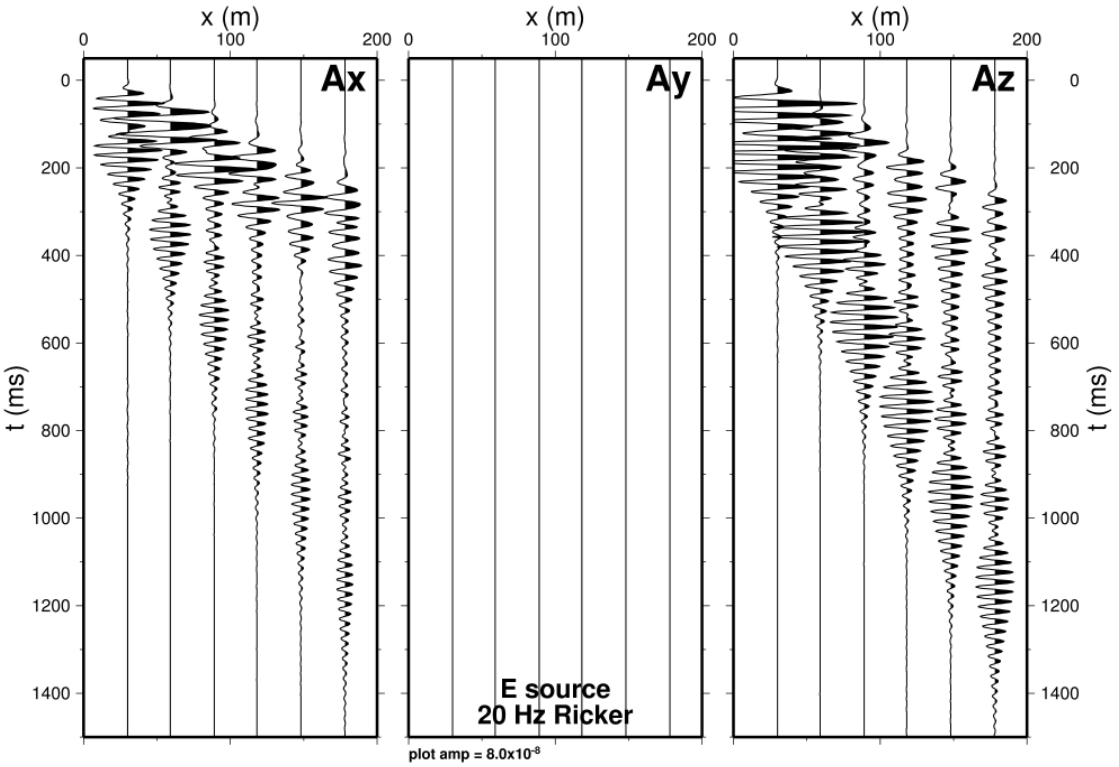

Figure 4.13. 3C particle acceleration traces generated by a shallow explosion (*E*) source activated by a 20 Hz Ricker wavelet.

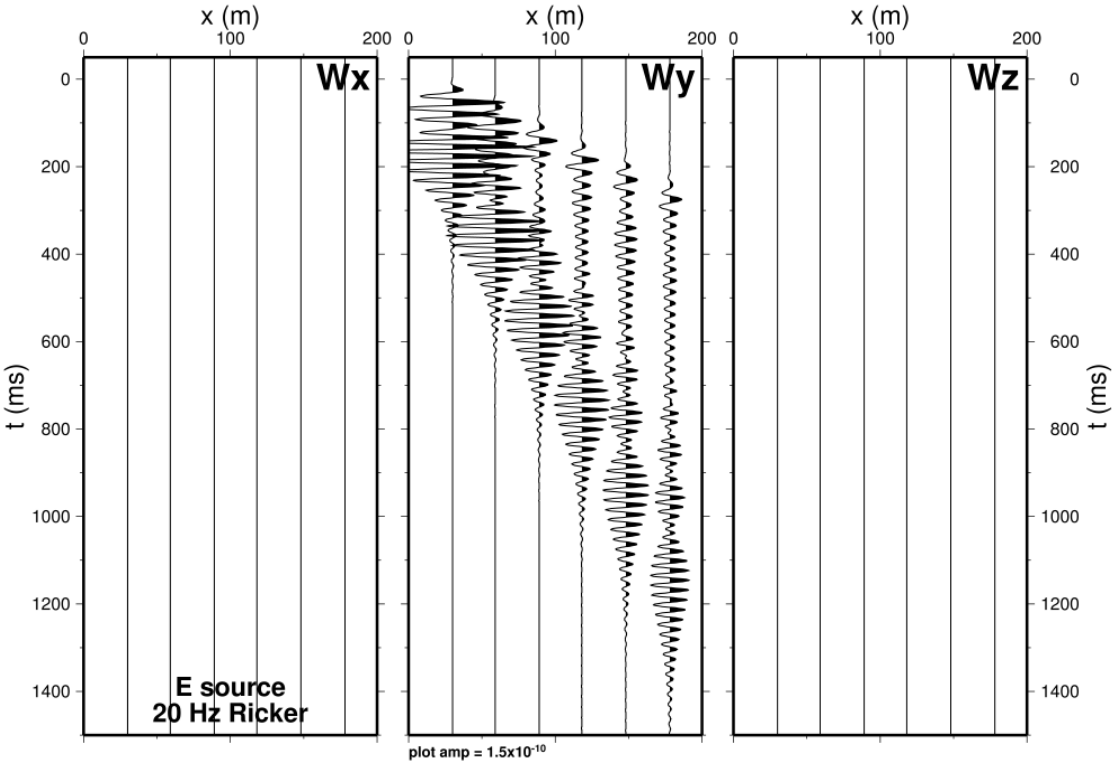

Figure 4.14. 3C particle rotation rate traces generated by a shallow explosion (*E*) source activated by a 20 Hz Ricker wavelet.

4.6 Point Seismic Array Results

The one-dimensional azimuth scanning algorithm described in section 3.1 is developed under extremely simple assumptions. In particular, we assume a plane shear body wave propagating within a homogeneous elastic wholespace. Both the propagation direction **n** and polarization **p** of the S-wave are horizontal (i.e., a horizontally-propagating SH wave). In this section, we deliberately apply the azimuth scanning algorithm to the more complicated synthetic seismic data calculated for the 1D layered Yucca Mountain earth model. Even though these data are dominated by a multi-component (i.e., simultaneous horizontal and vertical component motion) surface wave, the algorithm returns an excellent estimate of the azimuth angle to the source position!

Synthetic seismic data generated by the crossline (T_y) surface traction source are used for the analysis, since these data conform most closely to the assumptions underlying the scanning algorithm. As suggested by equation (3.4), we cross-correlated the *vertical* rotation rate (right panel of Figure 4.10) with the *horizontal* acceleration (center panel of Figure 4.9) rotated to a set of 360 candidate horizontal polarization directions. These directions are represented by the azimuth angle θ sampled in 1^o increments from 0^o to 360^o. The non-zero *horizontal* rotation rate component (left panel of Figure 4.10) is excluded from the cross-correlations. The zero-lag value of the cross-correlation function is retained and plotted against the candidate azimuth angle. An identical analysis is conducted for four different peak frequencies (10 Hz, 20 Hz, 30 Hz, and 40 Hz) of the Ricker wavelet source pulse used to generate synthetic seismic data.

The results generated by the simplified azimuth scanning algorithm are displayed in Figure 4.15 as curves of zero-lag cross-correlation coefficient *vs.* candidate azimuth angle. For each of the four source frequency spectra, the curve possesses a peak at $\theta = 180^o$, which is the back-azimuth angle to the known surface traction source position! Moreover, zero crossings of all curves are identical. We are extremely pleased (and remain somewhat mystified due to the simplifying assumptions adopted) by this result, which we consider highly significant. The simple azimuth scanning algorithm performs well with noise-free synthetic data calculated under circumstances that are much more complex than assumed in the mathematical derivation. In our opinion, this constitutes strong evidence supporting the feasibility of the point seismic array concept. The new result conveyed in Figure 4.15 is that higher source frequency content leads to a more sharply-peaked cross-correlation curve. In turn, this enables better resolution of the azimuth angle of the incident seismic radiation.

Figure 4.16 provides a simple test of our analysis in section 3.4 regarding frequency-independence of the inferred back-azimuth direction to the seismic energy source. Vertical rotation rate data generated with a Ricker source wavelet with a peak frequency of 10 Hz are cross-correlated against horizontal acceleration data generated by Ricker source wavelets of various peak frequencies (10 Hz to 40 Hz, in 10 Hz increments). One may think of the acceleration data as subject to an *additional* frequency filtering, induced either by the field sensor or intentionally during post-acquisition processing. Clearly, all cross-correlation coefficient curves still peak at the known back-azimuth angle $\theta = 180^o$. This is precisely the result predicted by our previous time-domain equation (3.21) or frequency-domain equation (3.22).

Our mathematical theory also suggests that the wavepseed of an incident shear wave may be determined by performing a scaling analysis of the horizontal acceleration and vertical rotation rate traces recorded at a single receiver station (see equation (3.14)). Results for the receiver located at offset distance 30 m for the Yucca Mountain synthetic data are displayed in Figure 4.17. Each plotted data point corresponds to the particular scalar $\hat{\beta}$ that minimizes the L1 norm misfit objective function (3.15) between A_y and W_z. This scalar constitutes an estimate of medium shear wave speed β. Frequency-dependence in β arises

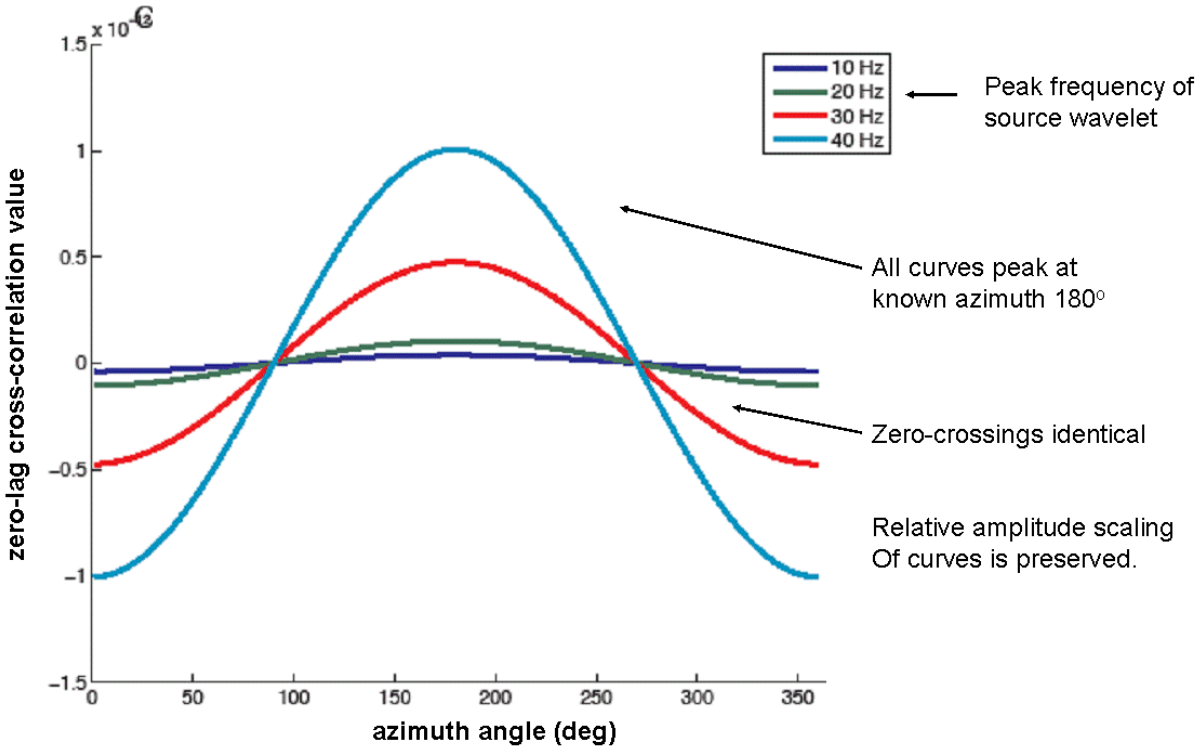

Figure 4.15. Zero-lag cross-correlation curves *vs.* candidate azimuth angle (in degrees) of incident wave propagation direction, calculated with synthetic seismic data obtained for the Yucca Mountain site. All curves possess a peak at $\theta = 180^{o}$, which is the back-azimuth angle to the known seismic energy source location. Color coding of curves indicates peak frequency of Ricker wavelet used to generate the synthetic seismic data.

because the seismic waves used in the analysis are a dispersive surface wave train. According to conventional seismological understanding, lower/higher frequency SH surface waves are sensitive to deeper/shallower shear wave structure. Thus, the results depicted in Figure 4.17 indicate that a surface wave dispersion curve may be obtained from seismic data observed at a *single* station, provided the appropriate measurements are made. A spatially-extended receiver array is not required.

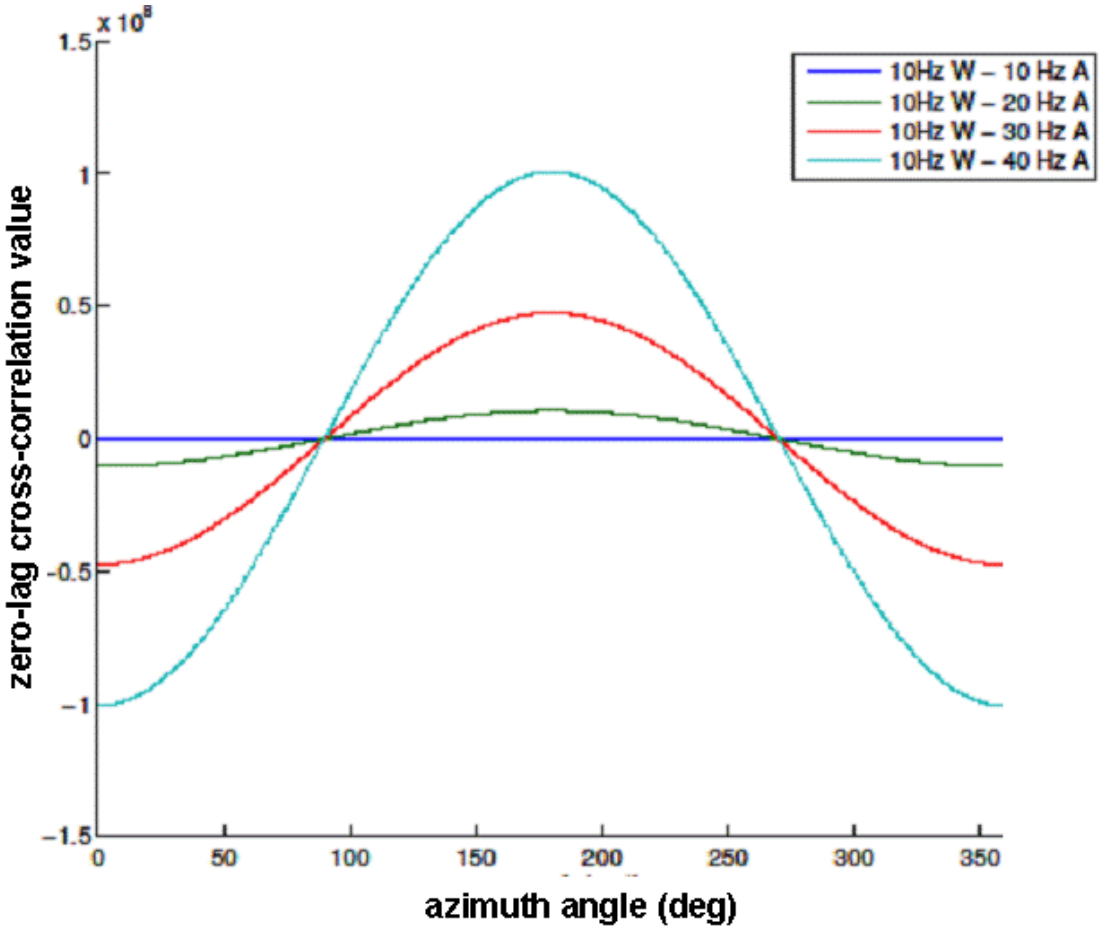

Figure 4.16. Zero-lag cross-correlation curves *vs.* candidate azimuth angle (in degrees) of incident wave propagation direction, calculated with synthetic seismic data obtained for the Yucca Mountain site. All curves possess a peak at $\theta = 180^{o}$, which is the back-azimuth angle to the known seismic energy source location. Curves are calculated by cross-correlating vertical rotation rate data generated with a Ricker wavelet with peak frequency of 10 Hz, with horizontal acceleration data generated by Ricker wavelets of various peak frequencies (10 Hz to 40 Hz).

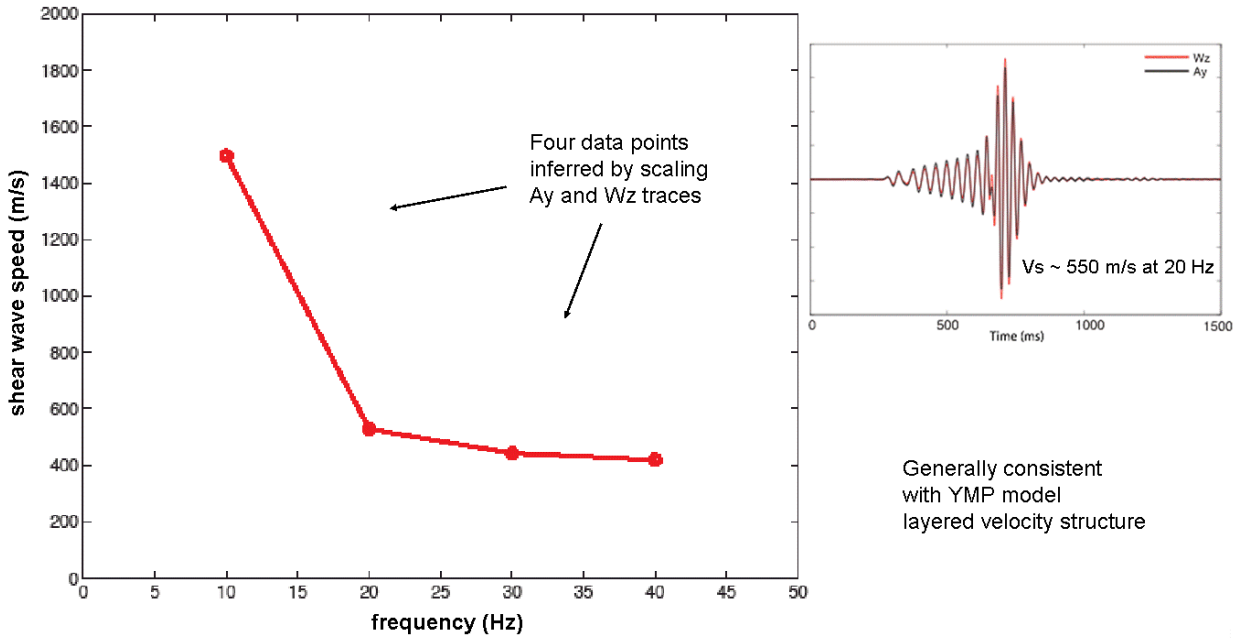

Figure 4.17. Dispersion curve of shear wave speed *vs.* frequency obtained by scaling co-located measurements of horizontal acceleration (A_y) and vertical rotation rate (W_z) measured at a single receiver station. Synthetic seismic data calculated for the Yucca Mountain layered earth model are used to obtain these results. Each frequency point corresponds to the peak frequency of a Ricker wavelet seismic energy source pulse. As frequency increases, inferred shear wave speed reduces, corresponding to shallower penetration depths of the surface wave train. Inset displays the remarkable agreement between A_y (black trace) and W_z (red trace) waveforms for the dominant source frequency of 20 Hz.

5.0 YUCCA MOUNTAIN FIELD DATA EXAMPLE

In this section, we apply the same simple azimuth scanning algorithm to seismic translational and rotational data acquired at the Yucca Mountain, Nevada site. Figure 5.1 shows the "T-Rex" three-component surface vibrator, owned and operated by the University of Texas, used as a seismic energy source.

Figure 5.1. **"**T-Rex" three-component vibrator seismic energy source at the Yucca Mountain, Nevada data acquisition site.

Power spectra of rotational seismic data recorded at source-receiver offset 30 m, both with and without the vibrator sweep in action, are plotted in Figure 5.2. The T-Rex vibrator generates energy significantly above the local ambient seismic noise level in the frequency range ~30 Hz to ~45 Hz.

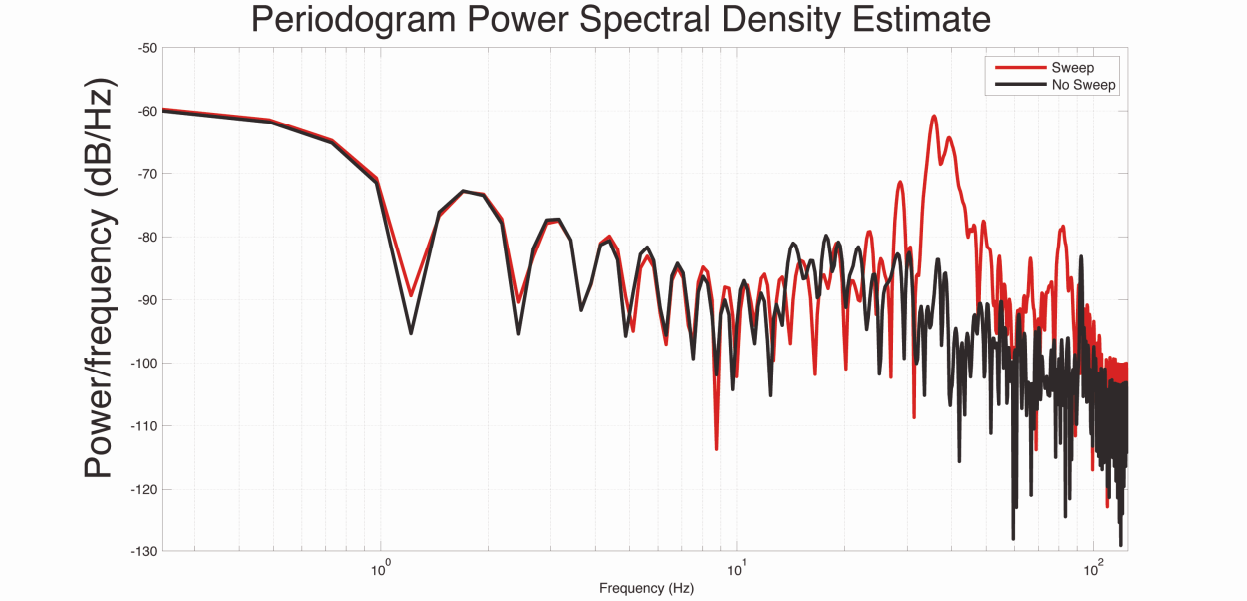

Figure 5.2. Power spectral density estimates obtained from seismic rotational recordings at the Yucca Mountain site, both with (**red** curve) and without (**black** curve) the T-Rex vibrator sweep activated.

Example rotational seismic data recorded at the site by the Eentec R1 sensor are displayed in Figure 5.3, as well as in Appendix B. The top panel illustrates vertical rotation rate (in radians per second) data recorded over a long-duration time window of 1200 seconds. When the T-Rex vibrator is actively sweeping, high-amplitude events are obvious. Conversely, when the vibrator is quiet, the rotation rate recordings display only some low-amplitude ambient noise events of unknown origin. The lower panel in Figure 5.3 displays zero-lag correlation coefficients obtained by cross-correlating horizontal acceleration with vertical rotation rate, over many short time windows. Each color-coded coefficient value (normalized to the range zero to unity) is plotted at the center time of the correlation window (horizontal axis) and with the inferred azimuth angle (vertical axis) of wave propagation. Red/blue colors indicate high/low coefficient values. Clearly, when the vibrator is active, the correlation values are large and tend to cluster about a fixed direction angle. In the absence of source activity, the low-value correlations do not display any preferred azimuthal alignment.

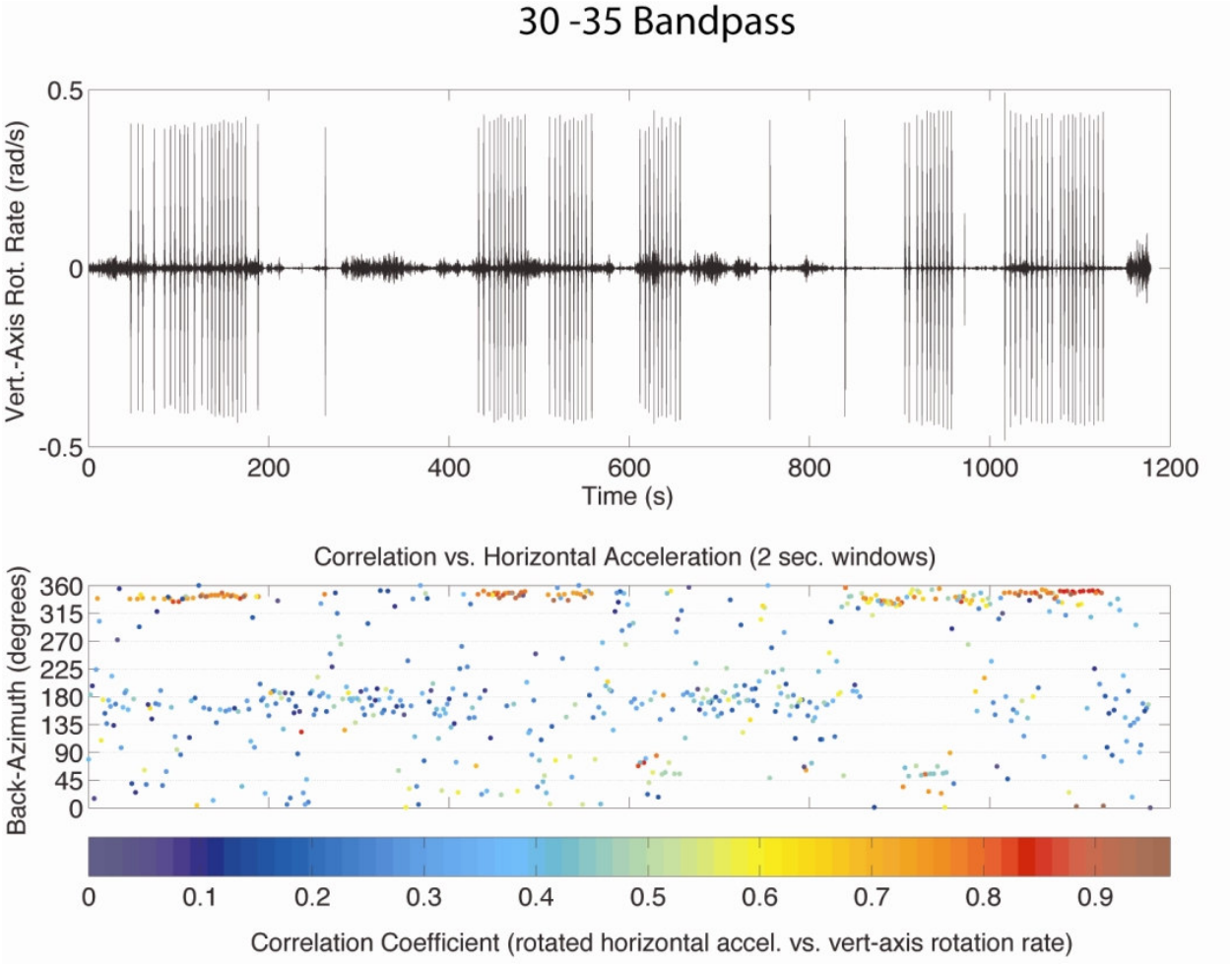

Figure 5.3. Top panel: vertical rotation rate data obtained at the Yucca Mountain field site over a recording window of 1200 seconds. Large amplitude bursts are generated by the T-Rex vibrator source. Lower panel displays zero-lag cross-correlation coefficients between "rotated" horizontal acceleration and vertical rotation rate. **Red**/**blue** colors indicate high/low coefficient values. High-value correlation coefficients tend to align along a fixed azimuth when the vibrator is active.

The limited results displayed in Figure 5.3 are encouraging. In order to test the viability of the azimuth scanning algorithm with field-acquired data, we engaged in extensive processing of the horizontal acceleration and vertical rotation rate data recorded at source-receiver offset 30 m at the Yucca Mountain site. Sixty-four high-amplitude vibrator events that occurred during a recording interval were analyzed. For each event, both data types were filtered with narrow bandpass Gaussian frequency filters, with peak frequency ranging from 1 Hz to 50 Hz, in 1 Hz increments. The filtered horizontal acceleration was rotated through 360° of azimuth angle, in 1° increments. For each candidate azimuth angle, the zero-lag cross-correlation coefficient with the observed (and frequency filtered) vertical rotation rate was obtained.

The extensive results are summarized in Figure 5.4. Clearly, over the frequency range from 30 Hz to 45 Hz where the vibrator energy source S/N ratio is high, the azimuth scanning algorithm obtains a *consistent* estimate of the wave propagation angle. Here consistency refers to 1) the high value of the correlation coefficient (red dots), and 2) minimal spread of the calculated azimuth angle. Outside of this frequency band, correlation coefficients tend to be low (blue dots) and the azimuth spread high.

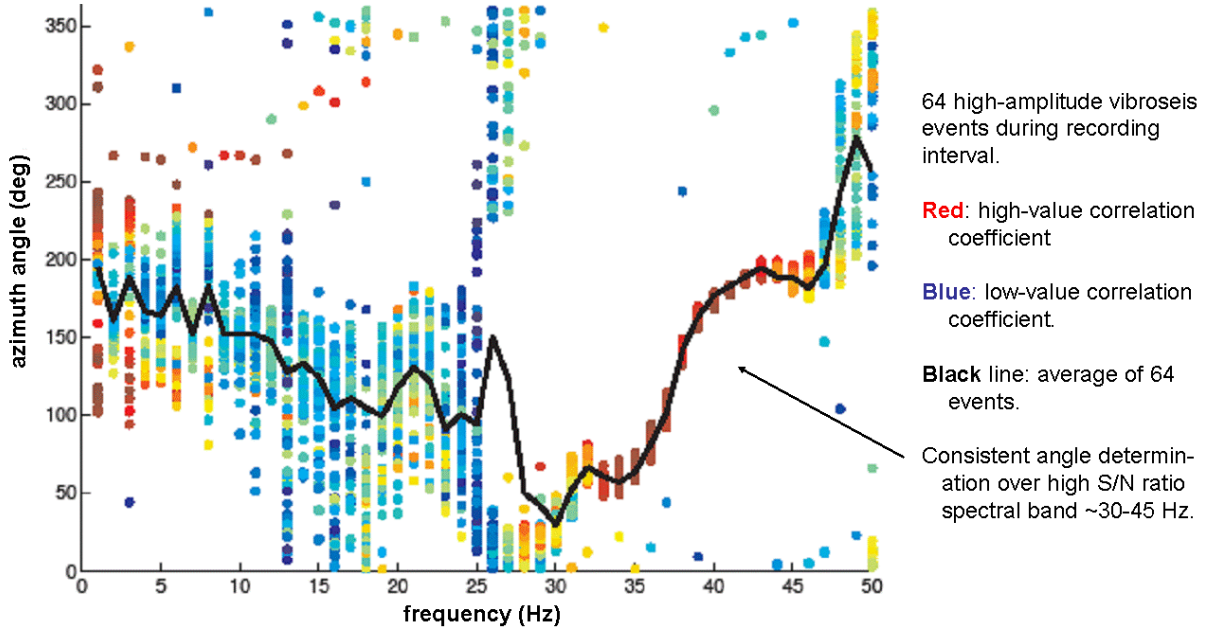

Figure 5.4. Wave propagation azimuth angle *vs*. frequency inferred from seismic data recorded at the Yucca Mountain site. "Frequency" refers to the peak value of a Gaussian-shaped bandpass filter applied to horizontal acceleration and vertical rotation rate data. For each of the 50 frequency bins, 64 inferred azimuth angle values are plotted, color-encoded according to the value of the zero-lag cross-correlation coefficient. **Red**/**blue** colors indicate high/low coefficient values.

The black curve in Figure 5.4 is the average azimuth angle calculated from the 64 high-amplitude vibrosesis events, at each of the 50 frequencies. An obvious question arises: Why does the inferred azimuth angle of incident wave propagation change with frequency? After all, the T-Rex vibroseis energy source remained fixed in place during this data acquisition experiment. We candidly state that we do not know the real reason for this phenomenon. However, there are two likely explanations:

1) Multiple seismic arrivals, with different propagation direction, are incident upon the co-located acceleration and rotation rate transducers. These events arise via reflection, refraction, scattering, etc. from three-dimensional geologic structure in the nearby subsurface. As the filtering frequency changes, the amplitudes of these events become more or less prominent, leading to different inferred azimuth angles. [Recall how the nature of the synthetic seismic data changed dramatically with source spectral content.] However, if the azimuth variation does result from this mechanism, we find it suprising that the estimated azimuth changes significantly over such short frequency intervals.

2) The unknown electromechanical response of the rotational sensor leads to a false, and frequency-dependent, azimuth estimation for incident seismic waves. Ideally, both the recorded acceleration and rotation data should be corrected for transducer response, so that subsequent cross-correlations can be conducted with valid approximations to actual ground motion. Unfortunately, the phase and amplitude responses of the Eentec R1 rotational sensor used for this experiment are not well known. Hence, we chose not to apply an instrument correction. We surmise that the uncompensated *phase response* of the Eentec R1 is generating a systematic error in azimuth angle over the frequency band 30 Hz to 45 Hz. Indeed, published phase response curves for the Eentec sensor (http://www.eentec.com/R-1_phase_new.htm) show variation on the order of 1 to2 radians over 10 Hz changes in frequency.

Despite this major ambiguity associated with the Yucca Mountain field seismic data, we feel that the consistency in inferred propagation azimuth angle in Figure 5.4, over the frequency range 30-45 Hz is a significant result.

6.0 CONCLUSION

A "point seismic array" consists of co-located three-component particle velocity (alternately acceleration) and particle rotation (alternately rotation rate) transducers. We have demonstrated, using a variety of mathematical, numerical simulation, and field data acquisition approaches, that a point seismic array is capable of inferring the type (P or S), direction, and speed of incident seismic waves. Future investigative efforts should involve:

1) Extending the mathematical and numerical simulation efforts to accommodate more realistic and complex seismic wave propagation scenarios (e.g., heterogeneous and/or anisotropic media, multi-component surface waves, interfering waves, noise).

2) Extending the azimuth scanning algorithm to three dimensions, and simultaneously improving the efficiency of the numerical cross-correlation methodology.

3) Engaging in more numerical simulation exercises in order to understand and quantify the "robustness' of the method.

4) Understanding the effects of transducer phase and amplitude responses on the calculated direction of wave propagation.

Finally, the encouraging results of this study strongly motivate efforts to improve the current crude state of rotational seismometry.

7.0 REFERENCES

Abbott, R.E., Aldridge, D.F., and Hart, D., 2007, Demonstration of the "point seismic array" concept with co-located rotatonal and translational sensors: American Geophysical Union Annual Fall Meeting, 10-14 December 2007, San Francisco, California, USA.

Aldridge, D.F., 1989, Statistically perturbed geophone array responses: Geophysics, **54**, 1306-1317.

Aldridge, D.F., 1990, The Berlage wavelet: Geophysics, **55**, 1508-1511.

Aldridge, D.F., 2000, Radiation of elastic waves from point sources in a uniform wholespace: Technical Report SAND2000-1767, Sandia National Laboratories.

Aldridge, D.F., Symons, N.P., and Haney, M.M., 2006, Finite-difference numerical simulations in seismic gradiometry: American Geophysical Union Annual Fall Meeting, 11-15 December 2006, San Francisco, California, USA.

Aldridge, D.F., and Haney, M.M., 2008, Numerical dispersion for the conventional-staggered-grid finite-difference elastic wave propagation algorithm: Technical Report SAND2008-4991, Sandia National Laboratories.

Ben-Menahem, A., and Singh, S.J., 1981, Seismic waves and sources: Springer-Verlag Company.

Schwaiger, H.F., Aldridge, D.F., and Haney, M.M., 2007, Full waveform 3D synthetic seismogram algorithm for 1D layered anelastic models: American Geophysical Union Annual Fall Meeting, 10-14 December 2007, San Francisco, California, USA.

Sheriff, R.E., 2002, Encyclopedic Dictionary of Applied Geophysics, Fourth Edition: Society of Exploration Geophysicists.

8.0 APPENDIX A – Predicted Magnitude of Seismic Rotation

The magnitude of seismic rotational motion is critical information for the design of a transducer possessing the requisite sensitivity. In this Appendix, plane wave analysis is utilized to estimate seismic rotation magnitude. It is emphasized that plane wave analysis is not overly restrictive, since a small portion of a geometrically-complex wavefront may always be considered a locally plane wave propagating within a locally homogeneous medium.

Consider a plane shear wave (i.e., with non-vanishing rotation) propagating in a uniform elastic medium with wavespeed $c = \beta$. The particle acceleration vector $\mathbf{a}(\mathbf{x},t) \equiv \partial\mathbf{v}(\mathbf{x},t)/\partial t$ and rotation rate vector $\mathbf{w}(\mathbf{x},t) \equiv \partial\mathbf{r}(\mathbf{x},t)/\partial t$ are

$$\mathbf{a}(\mathbf{x},t) = U\mathbf{p}w''\left(t - \frac{\mathbf{x}\cdot\mathbf{n}}{\beta}\right), \qquad \mathbf{w}(\mathbf{x},t) = -\frac{U}{\beta}(\mathbf{n}\times\mathbf{p})\,w''\left(t - \frac{\mathbf{x}\cdot\mathbf{n}}{\beta}\right), \tag{A1,2}$$

respectively. Recall that the unit polarization vector **p** for a plane shear wave is perpendicular to the unit propagation direction vector **n**. Combining these expressions gives

$$\mathbf{w}(\mathbf{x},t) = -\frac{1}{\beta}(\mathbf{n}\times\mathbf{p})\left[\mathbf{p}\cdot\mathbf{a}(\mathbf{x},t)\right]. \tag{A3}$$

Note that rotation rate has dimension "inverse time" (SI unit: s^{-1} or Hz). Taking the magnitude of this expression yields

$$\left\|\mathbf{w}(\mathbf{x},t)\right\| = \frac{1}{\beta}\left\|\mathbf{a}(\mathbf{x},t)\right\|. \tag{A4}$$

For typical geologic materials, the shear wavespeed may range from $\beta \le 1000$ m/s (for loosely consolidated soils), to $\beta \approx 2000$ m/s (for sediments), to $\beta \ge 3000$ (for consolidated sedimentary, igneous, or metamorphic rock). Hence, the above expression indicates that a shear wave rotation rate is about three orders of magnitude smaller than shear particle acceleration.

Thus, the problem of estimating magnitude of rotation rate reduces to estimating the particle acceleration associated with a propagating shear seismic wave. Of course, seismic accelerations vary over of vast numerical range, and depend on the seismic energy source magnitude, distance from source, and local elastic medium properties. Suppose that a strong seismic energy source (e.g., an earthquake) generates a near-field acceleration magnitude of 1 g $\approx$ 10 m/s^2 (there is some observed seismological evidence supporting this value). At a distance of 1 km = 1000 m, spherical divergence of the outward propagating wavefront (e.g., Aldridge, 2000) implies that this value is reduced by a factor of 10^{-3}, to 10^{-2} m/s^2. At a distance of 10 km = 10^4 m, acceleration magnitude diminishes to 10^{-3} m/s^2. Hence, a conservative estimate of a "typical" seismic acceleration might be about 10^{-6} m/s^2 (or ~10^{-7} g). If the shear wave speed β = 2000 m/s, then equation (A4) implies that the magnitude of rotation rate is approximately 5×10^{-10} Hz, or $\pi \times 10^{-9}$ radians/second.

Frequency Dependence

Equation (A4) indicates that the magnitude of rotation rate is proportional to the magnitude of acceleration. Hence, frequency scaling rules normally applying to particle acceleration also apply to

rotation rate. Suppose that the particle displacement waveform is a simple harmonic function with frequency f_0:

$$w(t) = \sin\left(2\pi f_0 t + \phi_0\right).$$

Then, the second derivative of $w(t)$ is

$$w''(t) = -\left(2\pi f_0\right)^2 \sin\left(2\pi f_0 t + \phi_0\right).$$

The maximum magnitudes of acceleration and rotation rate are

$$\max \left\|\mathbf{a}\left(\mathbf{x},t\right)\right\| = U\left(2\pi f_0\right)^2, \qquad \max \left\|\mathbf{r}\left(\mathbf{x},t\right)\right\| = \frac{U}{\beta}\left(2\pi f_0\right)^2,$$

respectively. Thus, increasing the frequency by a given factor (say 2), implies that acceleration and rotation rate are increased by the square of that same factor (or 4).

9.0 APPENDIX B – Example Eentec R1 Rotational Seismic Data

Two examples of rotation rate data acquired with the Eentec R1 rotational seismometer at the Yucca Mountain, Nevada site are displayed in this Appendix. The three-component R1 seismometer was deployed at a distance of ~30.0 m from the T-Rex vibrator seismic energy source depicted in Figure 5.1. The R1 was bolted to a flat metal plate emplaced directly on a sand/gravel roadside soil.

Data traces displayed below are short time windows extracted from a recording of much longer duration. Time sample interval is 4.0 milliseconds. A baseline drift (or trend) is removed from the long duration record, and recording system counts are converted to radians per second by dividing by the nominal R1 sensitivity of 50 Volts/radian/second. Each segment illustrates a prominent high-amplitude event generated by the vibrator.

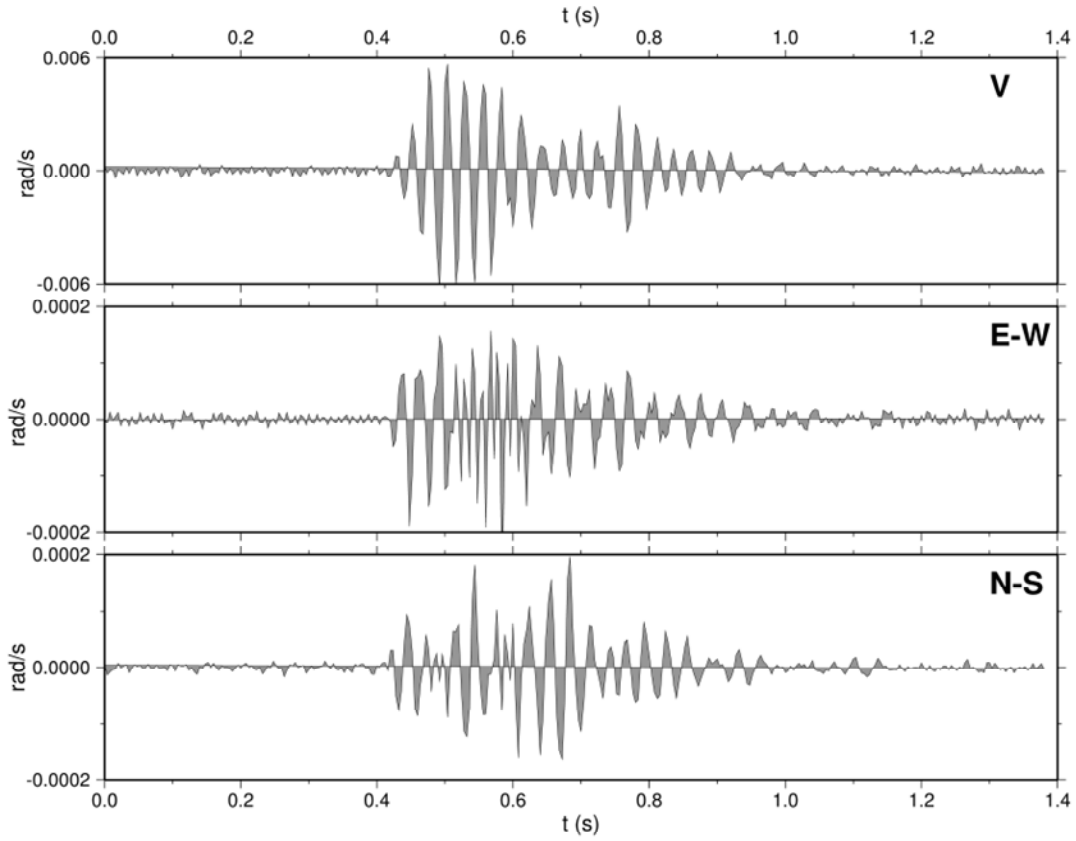

Figure 9.1. 1.4 second duration window of three-component (3C) rotation rate data (in radians per second) acquired at the Yucca Mountain field recording site. N-S and E-W refer to axes aligned *along* the north-south and east-west directions, respectively. Rotational motion should be understood as taking place *about* these axes. V refers to rotational motion about the vertical axis. The high-amplitude event is generated by the T-Rex vibrator approximately 30 m distant. Note that the amplitude of vertical rotation rate is approximately 30 times larger than horizontal rotation rate.

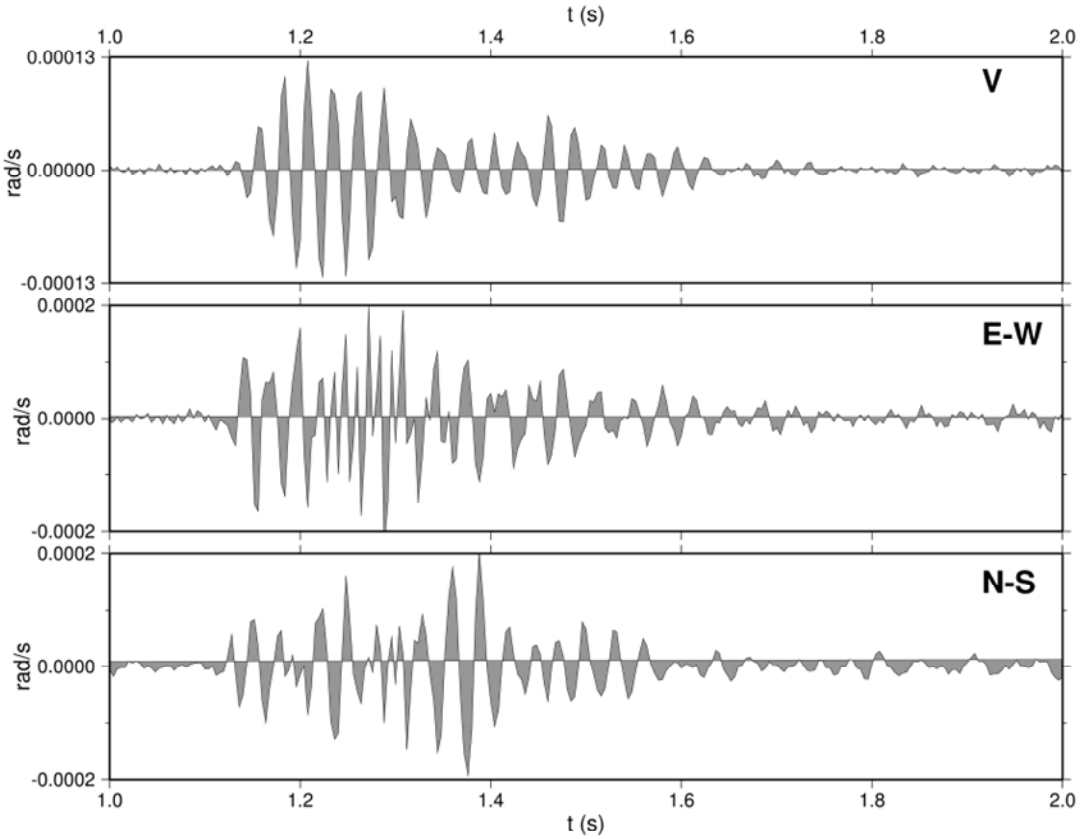

Figure 9.2. 1.0 second duration window of 3C rotation rate data (in radians per second) acquired at the Yucca Mountain field recording site. A different high-amplitude event generated by the T-Rex vibrator is displayed. The two horizontal rotation components (N-S and E-W) have the same amplitudes as in Figure 9.1. However, in this case, the amplitude of vertical rotation rate is only ~0.65 times the horizontal amplitude. The reason for this large difference in recorded vertical rotation rate amplitudes is presently not understood.

Frequency-domain amplitude spectra of the time-domain data displayed in Figure 9.1 and 9.2 are plotted in Figures 9.3 and 9.4, respectively. Amplitude spectra are normalized to unit maximum amplitude by dividing by the spectral value at the mode frequency f_{mode}, and plotted on a linear scale from 0.0 to 1.0. Frequency ranges from dc up to the Nyquist frequency of 125 Hz. Spectra in Figure 9.3 are obtained by directly Fourier transforming the data of Figure 9.1. However, Figure 9.4 is obtained by Fourier transforming a longer time window of the data displayed in Figure 9.2, although only the single prominent event of Figure 9.2 is contained within the analysis window.

There are clearly many common features shared by the spectra of Figures 9.3 and 9.4, for which we do not currently have adequate explanations. The main energy content appears to reside in the frequency range ~25 to ~40 Hz, although there is a gigantic spectral notch at ~32 Hz. All rotation components, but particularly the E-W component, possess substantial energy at about ~85 Hz. The reader is herewith left to ponder!

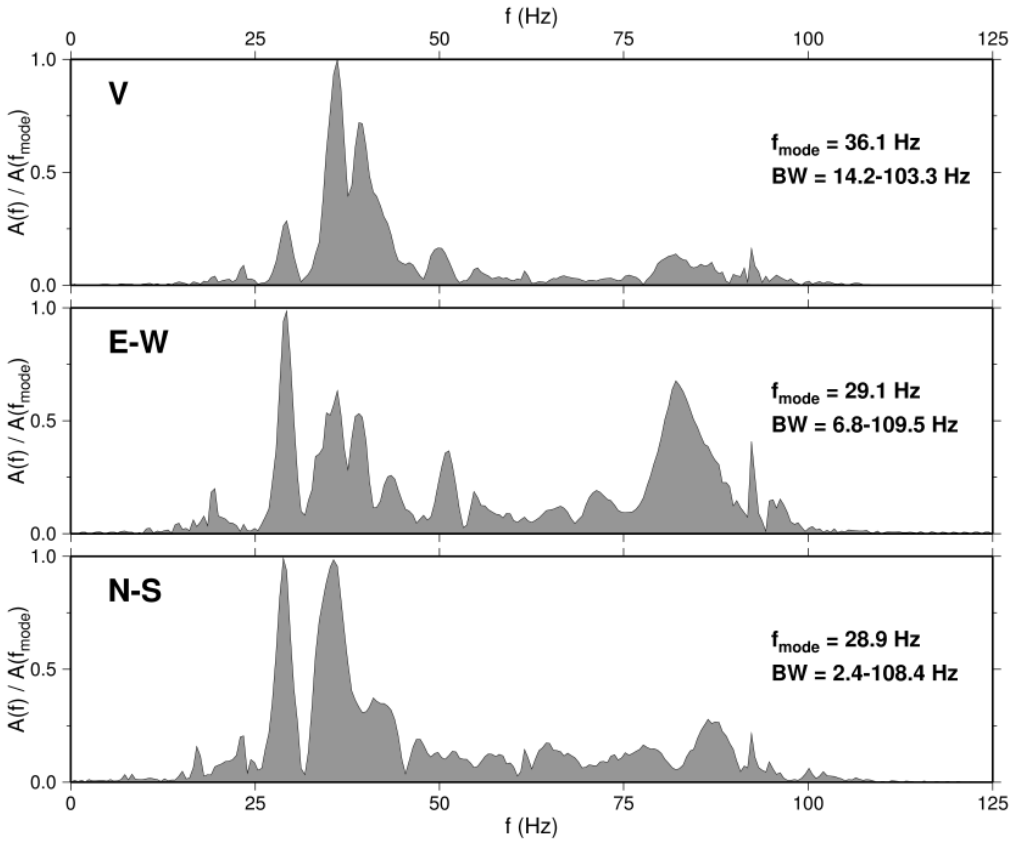

Figure 9.3. Frequency domain amplitude spectra of rotation rate traces displayed in Figure 9.1. Each spectrum is normalized to unit maximum amplitude by dividing by the spectral value at the indicated mode frequency. Bandwidth (BS) is specified at the 1% level of the normalized spectrum.

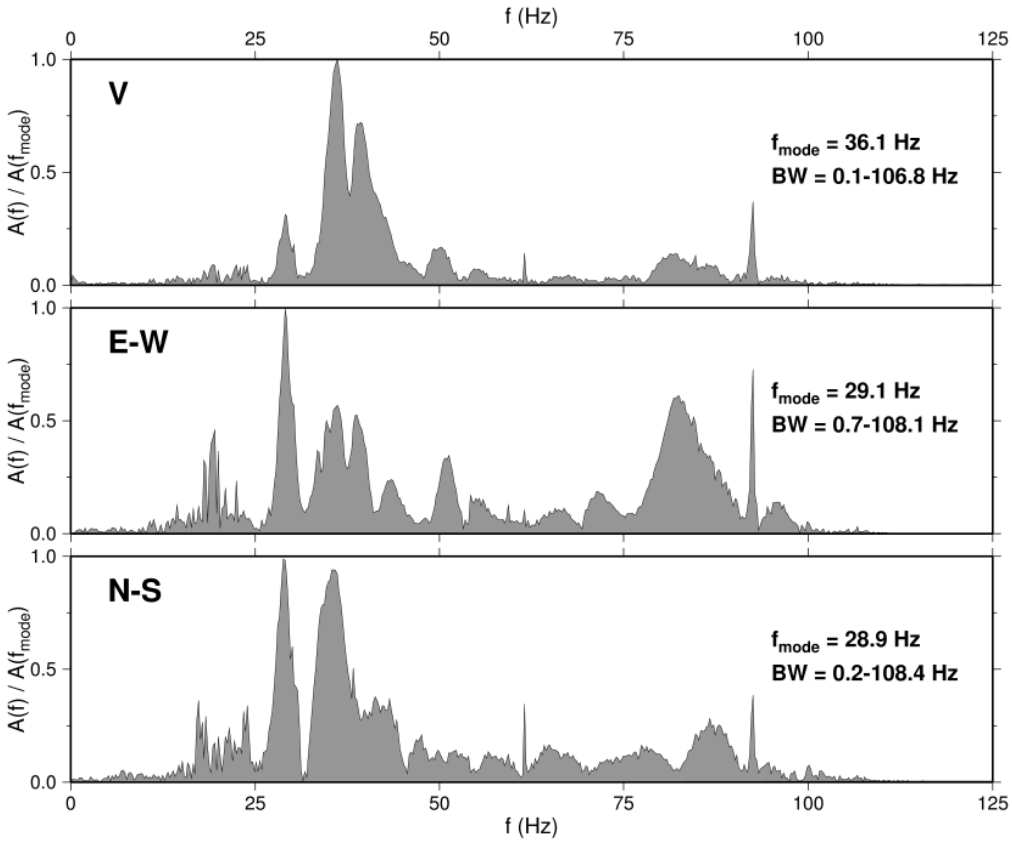

Figure 9.4. Frequency domain amplitude spectra of rotation rate traces displayed in Figure 9.2. Each spectrum is normalized to unit maximum amplitude by dividing by the spectral value at the indicated mode frequency. Bandwidth (BW) is specified at the 1% level of the normalized spectrum.

10.0 LIST OF FIGURES

11.0 DISTRIBUTION LIST

Sandia National Laboratories

D.F. Aldridge (3)	06314	MS 0750
R.E. Abbott (3)	01646	MS 1195
L.C. Bartel	06314	MS 0750
N. Bonal	06314	MS 0750
S.S. Collis	01416	MS 1320
G.J. Elbring	06314	MS 0750
D. Hart	05736	MS 0404
C.C. Ober	01433	MS 0316
L.A. Preston	06314	MS 0750
H.F. Schwaiger	06314	MS 0750
K.T. Stalker	05432	MS 1161
N.P. Symons	06314	MS 0750
B. G. Van Bloemen Waanders	01414	MS 1318
Technical Library (electronic copy)	09536	MS 0899

Other

R.H. Brune	Geophysical Consultant
M.M. Haney	United States Geological Survey
D. Hinkley	ExxonMobil Upstream Research Company


Sandia National Laboratories